MATERIALS SCIENCE

A general ink formulation of 2D crystals for wafer-scale inkjet printing

Guohua Hu[1,2]*, **Lisong Yang**[3]*, **Zongyin Yang**[1], **Yubo Wang**[1,4], **Xinxin Jin**[5], **Jie Dai**[6], **Qing Wu**[5], **Shouhu Liu**[1], **Xiaoxi Zhu**[1], **Xiaoshan Wang**[6], **Tien-Chun Wu**[1], **Richard C. T. Howe**[1], **Tom Albrow-Owen**[1], **Leonard W. T. Ng**[1], **Qing Yang**[4], **Luigi G. Occhipinti**[1], **Robert I. Woodward**[7,8], **Edmund J. R. Kelleher**[7,9†], **Zhipei Sun**[10], **Xiao Huang**[6], **Meng Zhang**[5‡], **Colin D. Bain**[3‡], **Tawfique Hasan**[1‡]

Recent advances in inkjet printing of two-dimensional (2D) crystals show great promise for next-generation printed electronics development. Printing nonuniformity, however, results in poor reproducibility in device performance and remains a major impediment to their large-scale manufacturing. At the heart of this challenge lies the coffee-ring effect (CRE), ring-shaped nonuniform deposits formed during postdeposition drying. We present an experimental study of the drying mechanism of a binary solvent ink formulation. We show that Marangoni-enhanced spreading in this formulation inhibits contact line pinning and deforms the droplet shape to naturally suppress the capillary flows that give rise to the CRE. This general formulation supports uniform deposition of 2D crystals and their derivatives, enabling scalable and even wafer-scale device fabrication, moving them closer to industrial-level additive manufacturing.

INTRODUCTION

The wide spectrum of distinct and yet complementary properties of two-dimensional (2D) crystals offers huge potentials for (opto) electronics, photonics, and sensor development (*1*, *2*). Engineering the 2D crystals also allows the fabrication of their hybrids and heterostructures, with an even more diverse set of properties for a substantially expanded application scope. In recent years, remarkable efforts have been devoted to adapting 2D crystals to functional printing toward their scalable and low-cost device fabrication (*3*). For this, the most common approach is to exfoliate their bulk crystals through chemical or ultrasonic assisted processes into mono- and few-layer flakes. These stably suspended dispersions are then directly used for device fabrication, showing glimpses of their exciting potential in recent advances (*4*–*6*). However, this direct adaption without elaborate ink formulation through control over composition, rheology, and fluidic properties presents challenges in achieving uniformly deposited functional structures and, hence, device reproducibility and scalability. The three critical parameters behind this are suboptimal droplet jetting (section S2), poor control over substrate wetting (section S2), and drying of the inks (Fig. 1, A to C). Although various approaches have been proposed to realize stable jetting and appropriate wetting (section S2), a strategy to suppress nonuniform deposition during drying of the deposited droplet, the coffee-ring effect (CRE), remains elusive.

The CRE in a drying droplet requires two essential conditions (Fig. 1I) (*7*, *8*): first, that the contact line is pinned and, second, that the droplet adopts a spherical-cap shape to minimize its surface-free energy. Simple geometric considerations then result in radially outward capillary flow to replenish solvent evaporating near the contact line. Note that capillary flow refers to Laplace pressure–driven flows of liquid arising from variations in the curvature of the liquid-air interface. Faster solvent evaporation at the contact line than at the apex enhances this capillary flow, which carries dispersed solutes to the contact line and deposits them there, leading to a ring-shaped stain. Because of this fundamental drying mechanism, suppression of the CRE is currently a major challenge in ink formulations of 2D crystals. Although various strategies have been developed to suppress the CRE (*9*, *10*), none of these are generally applicable for 2D crystal inks due to problems of dispersion stability, postprocessing requirements, or the effect of ink additives on material functionality. In particular, CRE-induced nonuniform deposition for additive-free 2D crystal inks is considerable on uncoated and nonporous substrates such as polyethylene terephthalate (PET) and Si/SiO$_2$.

Our previous discovery of uniform deposits of black phosphorus surmised that Marangoni effects, the flows caused by surface tension gradients, might be a determining factor to suppress the CRE in mixed alcohol inks (*11*). However, a detailed experimental understanding of the drying mechanism of these inks, key to the applicability of this approach to the wider 2D material family, was lacking. Here, with new experimental investigation, we present, to our knowledge, a new mechanism of natural suppression of the CRE and rationalize the exquisite sensitivity to the choice of the alcohols used (Fig. 1, D to H). We propose a general design principle for ink formulation to print uniform patterns of 2D crystals and their derivatives, enabling scalable manufacturing of planar functional devices such as gas sensors and photoconductors with highly reproducible properties.

[1]Cambridge Graphene Centre, University of Cambridge, Cambridge CB3 0FA, UK. [2]Department of Electronic Engineering, The Chinese University of Hong Kong, Shatin, Hong Kong. [3]Department of Chemistry, Durham University, Durham DH1 3LE, UK. [4]College of Optical Science and Engineering, Zhejiang University, Hangzhou 310027, China. [5]School of Electronic and Information Engineering, Beihang University, Beijing 100191, China. [6]Institute of Advanced Materials, Nanjing Tech University, Nanjing 210009, China. [7]Department of Physics, Imperial College London, London SW7 2AZ, UK. [8]MQ Photonics, Department of Engineering, Macquarie University, New South Wales, Australia. [9]Quantum Matter Institute, University of British Columbia, Vancouver, BC V6T 1Z4, Canada. [10]Department of Electronics and Nanoengineering, QTF Centre of Excellence, Aalto University, Tietotie 3, FI-02150 Espoo, Finland. *These authors contributed equally to this work.
†Present address: Department of Photonics Engineering, Technical University of Denmark, DK-2800 Kongens Lyngby, Denmark.
‡Corresponding author. Email: mengzhang10@buaa.edu.cn (M.Z.); c.d.bain@durham. ac.uk (C.D.B.); th270@cam.ac.uk (T.H.)
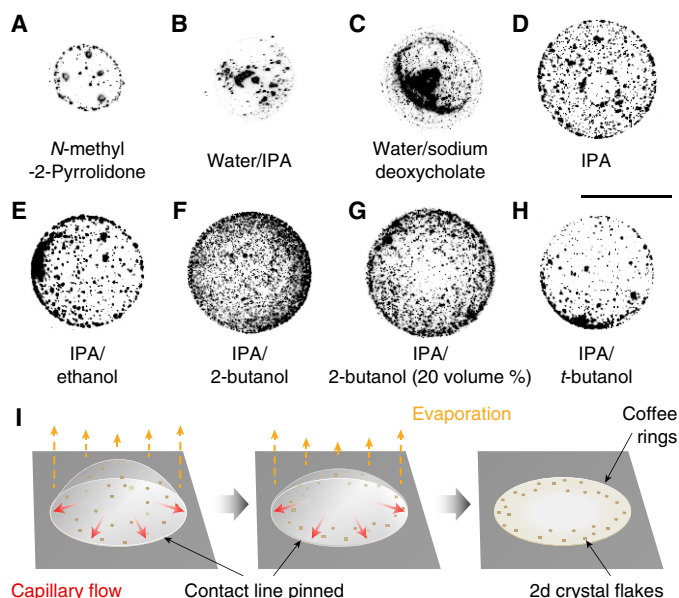
Fig. 1. Coffee-ring effect. Inverted optical micrographs of dried inkjet-printed droplets on clean glass: (**A** to **C**) common solution-processed 2D crystal dispersions (sections S1 and S2). (**D** to **H**) Formulated inks via solvent exchange in IPA or binary solvents of IPA/ethanol (10 volume %), IPA/2-butanol (10 and 20 volume %), and IPA/t-butanol (10 volume %). Scale bar, 50 μm. The brightness and contrast are optimized for clarity. MoS_2 is the 2D crystal example. Substrate is Si/SiO$_2$ at 60°C. (**I**) Schematic drying process showing CRE formation (8).

RESULTS

We investigate isopropanol (IPA)–based alcohol mixtures in our ink formulation. IPA is widely used as a solvent for graphics inks and, recently, for 2D crystal inks (3). It supports a metastable dispersion of the 2D crystal nanoflakes, and its low surface tension ensures good wetting of substrates (3). However, as we observe, ring stains persist with IPA-based 2D crystal inks (Fig. 1D). Binary mixtures of IPA with ethanol and t-butanol also produce nonuniform deposits, but a mixture of IPA with 2-butanol [optimally 10 volume percent (volume %)] suppresses the CRE (Fig. 1, E to H, and section S4). To understand the differing behaviors of the alcohol mixtures, we consider their surface tensions, γ, and evaporation rates (table S1). The blends are all zeotropic and show only small deviations from ideality. During drying, the concentration of the less volatile component is enhanced at the contact line. The radial surface tension gradient, dγ/dr, for IPA/ethanol is <0 (ethanol evaporates faster, enriching the contact line with lower surface tension IPA), >0 for IPA/2-butanol, and ≈0 for IPA/t-butanol (similar volatilities).

To visualize the flows arising from these surface tension gradients, we seed IPA and the blend droplets with polystyrene tracer particles (Fig. 2, section S3, and movies S1 to S4). Radially outward flows with no recirculation are observed in all these droplets. Plots of the particle trajectories show that IPA, IPA/ethanol, and IPA/t-butanol behave similarly, but IPA/2-butanol is markedly different (Fig. 2, B and C). In the first three cases, the droplets are pinned at the early stage of drying, <0.1 t_f (where t_f is the drying time); the particle velocities are greatest when close to the contact line and increase during drying. The IPA/2-butanol droplet, however, continues to expand until 0.36 t_f with particles near the contact line moving at the same speed as the

contact line; after the droplet ceases to expand, the particle velocities reduce greatly.

Tracer particles perturb flows when the height of the droplet approaches the diameter of the particles (12). Therefore, we also study the spreading and drying behavior of these four solvent systems without the tracer particles (Fig. 2D). In all the cases, the droplets dissipate their kinetic energy ≈ 1 ms after impact (13) and spread in diameter during 0.01 t_f to 0.03 t_f following a power law, $D \approx t^n$ with $n \approx 0.14$, slightly larger than the value of 0.1 expected from Tanner's Law when the gravitational force is negligible due to droplet size (14). IPA, IPA/ethanol, and IPA/t-butanol then show a long and slow retraction of the contact line, following $D \propto (t_f - t)^n$ with $n = 0.52 \pm 0.01$ during drying phase of 0.68 t_f to 0.97 t_f (section S3 and fig. S4), close to the value of 0.5 expected for diffusion-limited evaporation with a constant contact angle (15). These three fluids follow theoretical "universal curves" for evaporation of a pure wetting fluid in the absence of thermal Marangoni effects (16). This agreement does not prove that thermal Marangoni effects are not present but shows that they do not noticeably influence the drying dynamics. The consonance of the three curves demonstrates further that solutal Marangoni effects do not influence the shape evolution in the IPA/ethanol or IPA/t-butanol mixtures.

In lubrication theory (17), the evolution equation for the droplet height, h, depends on a dimensionless parameter, $C = \varepsilon^3/3Ca$, where the capillary number $Ca = \eta u/\gamma$ (where ε is the aspect ratio h_0/R_0, η is the viscosity, u is the characteristic radial velocity, and γ is the surface tension). C represents the relative importance of height changes due to flows caused by differences in Laplace pressure (capillary flows) and those due to evaporation. When $C \gg 1$, capillary flows readily balance the loss of liquid by evaporation, and the droplet shape remains close to a spherical-cap. Conversely, when $C \ll 1$, capillary flows are negligible, and the height evolution is determined by the local evaporation rate (in the absence of Marangoni effects). For these three cases, we find $C = 10$ at the beginning of spreading [where we have taken h_0 and R_0 to be the height and radius immediately after impact ($t \sim 1$ ms; ε ~ 0.18) and u to be the contact line speed of 2.4 mm s^{-1}], $C = 2$ at maximum spreading, and $C \sim 1$ during the retraction phase. Although C is not always ≫1, side-view measurements of the droplet profile at early times and interferometric profiles at later times show that the droplet profile is always well-fitted by a spherical-cap (section S3 and fig. S4). In the presence of particles that pin the contact line, capillary flows are expected to lead to ring stains (7, 8), which is what we observe (Fig. 1).

The IPA/2-butanol mixture shows remarkably different dynamics after the initial spreading phase ($t < 0.05$ t_f). The droplet continues to spread for about 60% of the drying time, at an almost constant speed, followed by a sharp transition into rapid contact line retraction. The retraction does not follow a power law (fig. S4). Reconstructed profiles show that IPA/2-butanol changes from the initial spherical-cap into a flattened pancake shape as early as 0.33 t_f, which persists through the remainder of drying (Fig. 2E). Immediately after impact, the value of C is similar to that of the other three solutions; the very different spreading behavior shows that there must be additional terms in the height evolution equation. Once the droplet adopts a pancake shape, the curvature is small, resulting in an absence of Laplace pressure gradients to drive radial flow (except in close proximity to the contact lines). Consequently, the droplet thins uniformly as it evaporates, leading to a uniform deposit. The dominance of evaporation over capillary flows can also be inferred from
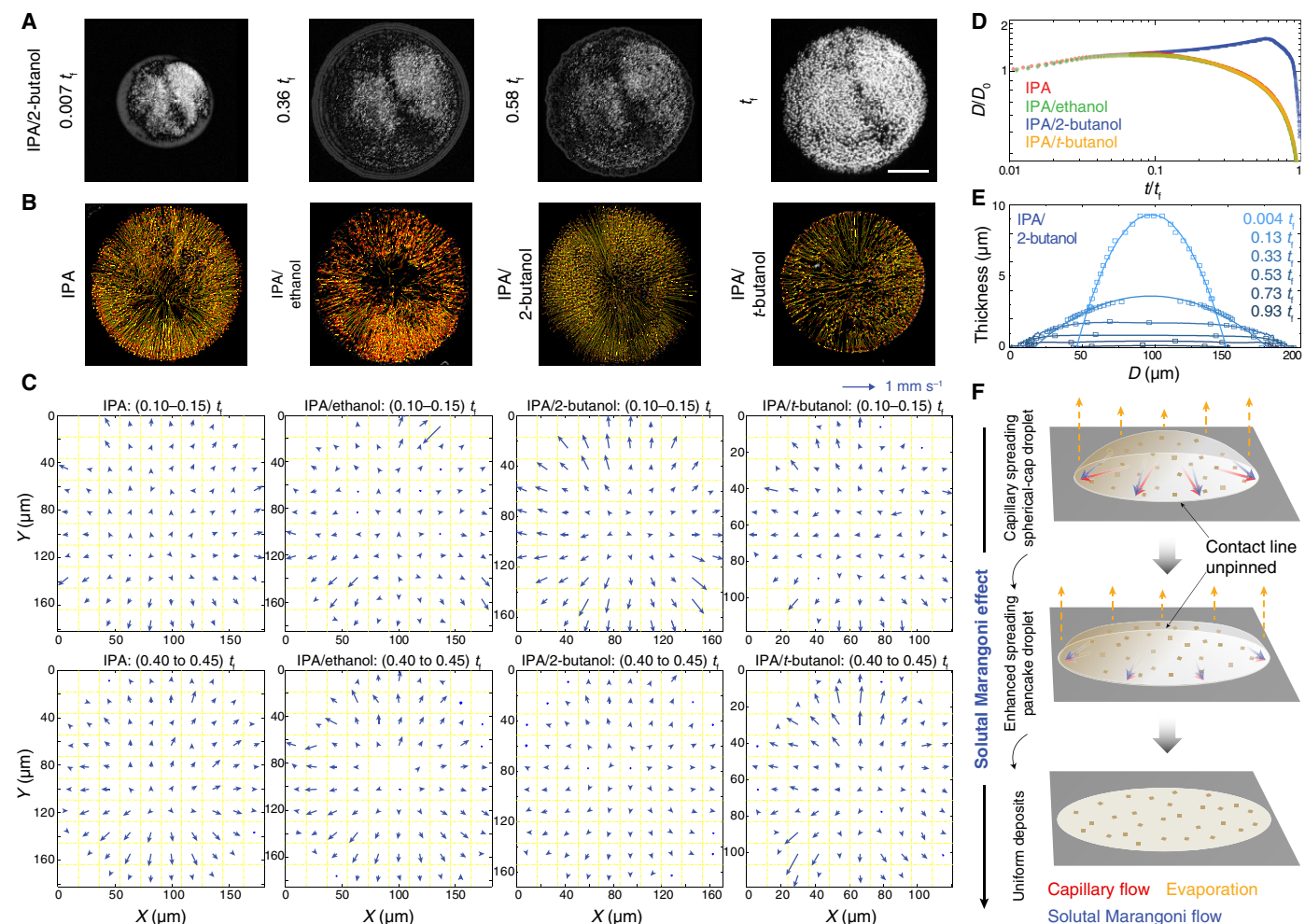
Fig. 2. Solutal Marangoni effect. (**A**) Optical micrographs of a drying droplet of IPA/2-butanol (10 volume %) with tracer particles on glass from droplet impact (0.007 t_f), to maximum spreading (0.36 t_f), to when the edge recedes close to the particle periphery (0.58 t_f), and at the end of drying (t_f). Scale bar, 50 μm. The brightness and contrast are optimized for clarity. (**B**) Particle trajectories at 0.04 t_f to 0.05 t_f, with red arrows showing the trajectory end, and (**C**) the corresponding velocity maps averaged over two time intervals: For IPA, IPA/ethanol, and IPA/t-butanol, the particles nearest to the pinned contact lines display largest velocities and increase from ~0.3 to ~0.6 mm s^{-1}; for IPA/2-butanol, the contact line and the near particle first advance at ~0.5 mm s^{-1}. The droplet then ceases to expand, and the particle velocities greatly decrease. Polystyrene nanoparticles (diameter ~755 nm) are used as tracer particles as 2D crystals are too small to visualize. Stationary particles adhering to substrates are excluded from analysis. (**D**) Contact diameter (D) of droplets without tracer particles as a function of time. The time is normalized by t_f and D by the diameter just after (1 ms) inertial droplet impact (D_0). (**E**) Reconstructed height profiles of an IPA/2-butanol droplet at various times (movies S6 and S8). Solid line at 0.004 t_f and 0.13 t_f is circular fit. (**F**) Schematic depicting the solutal Marangoni effect.

a calculation of C for the pancake shaped droplets; if we use droplet properties half-way through drying, we find $C = 10^{-2}$, which is << 1.

We propose that CRE suppression in IPA/2-butanol arises from solutal Marangoni-enhanced spreading (Fig. 2F) (*18–20*). After the initial capillary-driven spreading ($t < 0.05\ t_f$; Fig. 2D), spreading is strongly coupled with drying until 0.6 t_f. Faster evaporation of IPA enriches the contact line with 2-butanol, leading to a surface tension gradient acting from the droplet apex to the contact line. This shear stress accelerates the radially outward spreading flow, as shown in the velocity map in Fig. 2C. The surface tension gradient can be estimated from the velocity gradient: We estimate the difference in the surface tension between the apex and contact line as O(10^{-5} Nm^{-1}), only 1% of the surface tension difference between the two solvents (section S3). In Marangoni-driven spreading, the velocity at the free surface is twice the mean of radial velocity. The nanoparticle-enriched

zone at the (moving) contact line is constantly overtaken by fresh solution from the center, maintaining a uniform concentration profile. The persistence of the pancake shape during drying can be understood qualitatively as follows. For small Peclet numbers, the composition of the droplet is uniform with height. The rate of change of composition with evaporation is inversely proportional to the thickness of the film. Consequently, thicker areas of the drop are richer in IPA and, therefore, have a lower surface tension than thinner areas, leading to a Marangoni flow from thicker areas to thinner areas. We propose that this natural negative feedback mechanism assists the suppression of the CRE. We note that the thermo-Marangoni effect on suppression of the CRE is negligible (*21*) and has been discussed in section S3.

With this mechanistic understanding, we synthesize >10 different 2D crystals, their heterostructures (solution grown 2D-2D material
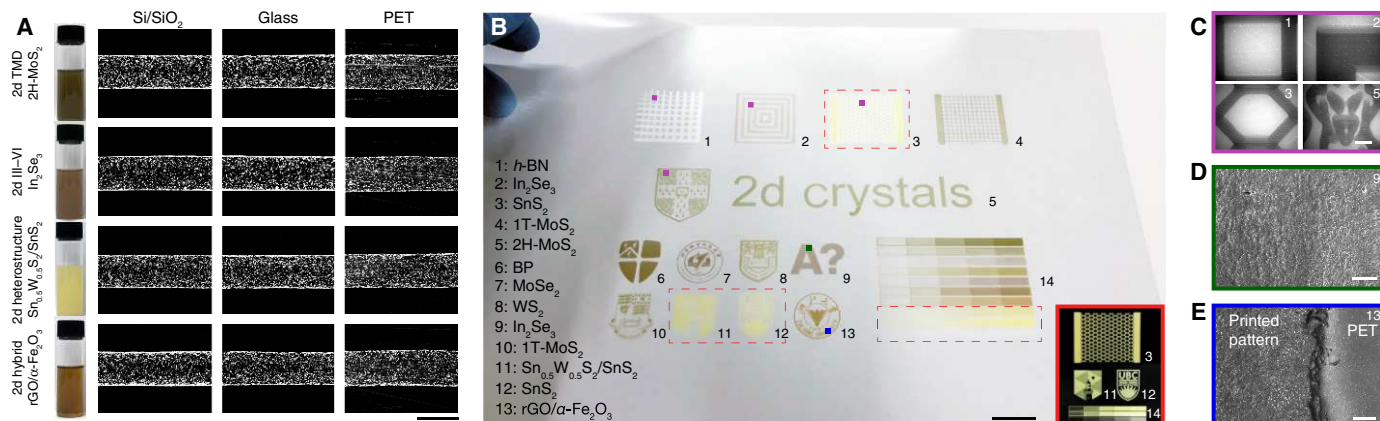
Fig. 3. Inkjet printing of 2D crystals. (**A**) Ink examples and corresponding optical micrographs of printed single lines on Si/SiO$_2$. Scale bar, 100 μm. The inks are diluted for clarity. Brightness and contrast of the lines are enhanced to reflect the distribution of printed flakes. TMD, transition metal dichalcogenide; *h*-BN, hexagonal boron nitride. (**B**) Printed patterns on PET: (1 to 13) individual patterns and (14) gradient printing. Scale bar, 1 cm. Inset shows 3, 11, 12, and 14 with a dark background. Corresponding (**C**) optical micrographs of selected areas in 1, 2, 3, and 5. Scale bar, 500 μm. (**D** and **E**) SEM in 9 and 13. Scale bars, 100 μm. Photo credit: Guohua Hu, University of Cambridge and The Chinese University of Hong Kong.

systems) and hybrids (solution grown 0D-2D material systems), and formulate their inks (section S4 and fig. S5). We present inkjet printing of these inks in Fig. 3. Uniform flake distributions are achieved across all the printed single lines on the substrates (Fig. 3A), underscoring the ability of our inks to suppress the CRE. The optical absorbance measured from the printed patterns linearly scales with the print repetition (errors <2.5%; fig. S9). The pattern-to-pattern variation is also minimal (errors <5%; fig. S10), underscoring highly controlled and uniform printing achievable with our inks. The printing process can be scaled up for large-area patterning (Fig. 3B). Figure 3C presents the corresponding high-resolution optical micrographs of selected areas, demonstrating that the patterns are uniform without CRE. Close-up examination through scanning electron microscopy (SEM) also confirms this (Fig. 3, D and E). In particular, Fig. 3E shows sharp, clear edges of the prints in spite of prolonged print sessions involving 60 print repetitions. The ink formulation is applicable for other material systems, for example, nanoparticles (e.g., polystyrene nanobeads) and organic salts (e.g., oxalates; fig. S6). We propose the formulation may also be suitable for ink pigment particles in a similar size range if stable suspension can be achieved. The inks can also be spray coated for highly uniform coating (section S5 and fig. S7).

With regard to the previous printed 2D crystal device demonstrations, there have been two primary obstacles for real-world applications. First, the current solution-based synthesis or processing of 2D crystals limits their properties compared to those produced via alternative methods. This is primarily due to the smaller and irregular flake dimension inherent to solution processing techniques. This typically translates to inferior performance metrics in devices such as transistors or photodetectors, compared to those produced from mechanical exfoliation or high-temperature synthesis of 2D crystals. The second challenge is the consistency in the device performance as a result of nonuniform printing of 2D crystals, largely due to the CRE. Printed planar devices leveraging the properties of solution-processed 2D crystals, such as gas sensors, hold enormous application potential if such performance variabilities are addressed. This demands considerable innovations in the underlying ink formu-

lation strategies. Our work focuses on the solvent carrier design. In this work, we exploit our ink formulation to address the second challenge and investigate the device-to-device variabilities of three types of inkjet-printed 2D crystal devices. However, we note that the CRE may not necessarily be independent of the dimension of the 2D crystal nanoflakes and that enhanced control of the dimensions may be exploited to refine their interparticle capillary interactions for additional CRE suppression (*22*).

As demonstrations, here, we print arrays of nonlinear optical saturable absorbers (SAs; 4 × 8 array), room temperature gas sensors (5 × 10 array), and photodetectors (45 × 100 array) with 2H-MoS$_2$ and 2D hybrid rGO/α-Fe$_2$O$_3$ (Fig. 4). These 2D crystals, especially in their solution-processed forms, are widely used in these applications (*1*, *23*, *24*). Assessment of 16 randomly selected SAs shows uniform duration of the ultrafast pulses generated, fitting a Gaussian distribution with 3.3% spread in SD (σ) from the mean (μ; Fig. 4C). Likewise, the printed room temperature NO$_2$ sensors and photodetectors show a respective spread of 2.5% (Fig. 4G) and 9.1% in their response (Fig. 4L). See sections S7 to S9 for further details. These narrow spreads are substantially lower than what can be achieved with the solution-processed N-methyl-2-pyrrolidone (NMP)–based dispersions (fig. S14). In comparison, depending on the complexity of the circuit, a variation of ±10 to ±30% in threshold voltage in printed thin-film transistors is considered acceptable for passive radio frequency sensors in an industrially scalable printing process (*25*). Our reported narrow spreads in performance are therefore well within acceptable statistical variations for printed device manufacturing from 2D crystal inks, addressing one of the most challenging obstacles toward their additive manufacturability.

DISCUSSION
Through experimental observations, we have introduced a new drying mechanism that uses Marangoni-enhanced spreading to suppress the CRE through contact-line unpinning and droplet deformation. Exploitation of this formulation for inkjet printing of 2D crystals enables scalable device fabrication, with highly consistent and
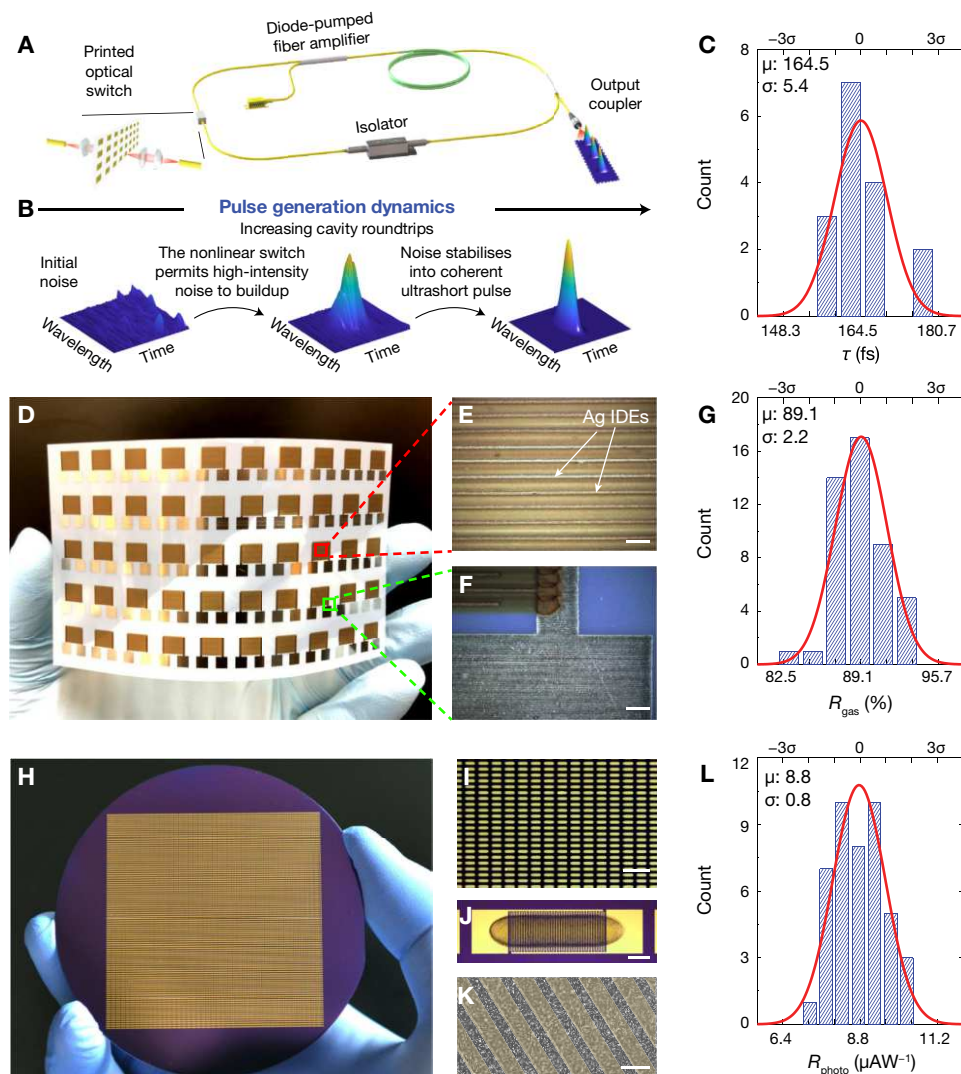
Fig. 4. Inkjet-printed patterns with identical print-to-print functional features. (**A**) Schematic of ultrafast fiber laser cavity showing integration of an array of 4×8 inkjet-printed 2H-MoS$_2$ SAs. (**B**) Spectrogram plots illustrating the evolution of ultrashort laser pulse generation. (**C**) Gaussian fitting of the measured pulse duration τ of randomly selected 16 SA devices. (**D** to **F**) Fully inkjet-printed rGO/α-Fe$_2$O$_3$ 5×10 sensor array on PET. Scale bars, 100 μm. Photo credit: Guohua Hu, University of Cambridge and The Chinese University of Hong Kong. (**G**) Gaussian fitting of the measured responsivity (R_{gas}, the change in the device resistance) of at 1 part per million NO$_2$. Three short-circuited devices are excluded from fitting. (**H**) Photograph of 100×45 inkjet-printed MoS$_2$ photodetector array on a 3-inch wafer (diameter 76 mm), where the uniformly printed 2H-MoS$_2$ over interdigitated gold electrodes acts as the active layer. Photo credit: Yubo Wang, University of Cambridge and Zhejiang University. (**I**) Photograph of >300 devices, showing visually identical printed MoS$_2$ array. Scale bar, 2 mm. (**J**) Optical micrograph of a single photodetector. Scale bar, 100 μm. (**K**) SEM micrograph showing even flake distribution over the false-colored interdigitated electrodes. Scale bar, 10 μm. (**L**) Gaussian fitting of the measured responsivity R_{photo} of a randomly selected 50-device array under 40-μW illumination at 635 nm, 5 V. Six devices are short-circuited and excluded from the fitting.

reproducible properties. Further understanding of this mechanism could allow adaptation of solvent mixtures beyond those investigated here, considerably expanding its applicability for the wide range of 2D crystals and other material platforms, including nanoparticles and organics. Reliable printing of such a wide range of optically and electrically active materials and their mixtures will substantially boost the fabrication of complex emerging devices. Our ink formulation with active CRE suppression thus lays the foundation for high-speed additive manufacturing of all-printed sensors and systems with a high level of large-scale integration.

MATERIALS AND METHODS
Solution processing methods
The 2D crystal flakes, including graphene, transition metal dichalcogenides [molybdenum disulfide (MoS$_2$), molybdenum diselenide (MoSe$_2$), and tungsten disulfide (WS$_2$)], hexagonal boron nitride (h-BN), bismuth telluride (Bi$_2$Te$_3$), indium selenide (In$_2$Se$_3$), and black phosphorus (BP), are produced via previously reported liquid-phase exfoliation, ion intercalation, and chemical synthesis. The 2D crystal heterostructure (solution-phase epitaxy grown Sn$_{0.5}$W$_{0.5}$S$_2$ nanoplates onto SnS$_2$ nanoplates, Sn$_{0.5}$W$_{0.5}$S$_2$/SnS$_2$) is produced via solution-based

epitaxy. The graphene hybrid (reduced graphene oxide with spindle-like α-Fe_2O_3, rGO/α-Fe_2O_3) is synthesized via hydrothermal method. See detailed solution processing methods and the material characterizations in section S1.

Droplet-drying study

Details of the setups and the analysis of the radial flows of sessile droplets and their spreading and drying are available in section S3.

Ink formulation and characterization

The produced 2D crystals are redispersed in mixtures of IPA and alcohol (anhydrous alcohols for BP) through 10-min sonication for ink formulation. The ink concentration is adjusted to 1 g liter^{-1}. The 1 T-MoS_2 ink contains 9 volume % water to stabilize the flakes. Polystyrene nanobead solution (10 weight %; Sigma-Aldrich) is diluted with IPA/2-butanol (10 volume %) by 50 times for ink formulation. N,N,N',N'-tetramethyl-4,4'-diaminotriphenylcarbenium oxalate (Sigma-Aldrich) is dissolved in IPA/2-butanol (10 volume %) at a concentration of 5 g liter^{-1} for ink formulation. The typical surface tension, viscosity, and density of the inks are 28 mNm^{-1}, 2 mPas, and 0.8 gcm^{-3}, respectively, giving an inverse Ohnesorge number of 10. This ensures stable jetting of individual droplet corresponding to each electrical drive pulse. Commercial silver ink (Sigma-Aldrich) is used as received for printed Ag interdigitated electrodes (IDEs) for the gas sensors.

Inkjet printing and characterization

Fujifilm Dimatix Materials Printer DMP-2831 is used. The ink cartridge is Dimatix DMC-11610, with a jetting nozzle diameter of 22 μm. The volume of individual droplets generated is 10 pL. For a typical printing process, the substrates [Si/SiO_2 (oxide thickness of 100 nm), glass, and PET (thickness of 50 μm)] are cleaned with acetone/IPA/deionized water before printing. For printing of the SAs, a 1.5-μm-thick PET is used as provided. For ease of handing, this PET is laminated onto a 100-μm-thick PET support before printing; it can be easily peeled off for device integration after printing. For printing of the sensors, a PET substrate with porous coating (Mitsubishi) is used as received. To prevent buildup of agglomeration of 2D crystals around the nozzles, cleaning is conducted via purging the nozzles with an IPA/2-butanol mixture before and after each print repetition. For SEM characterization of inkjet-printed 2D crystals, a ~6-nm-thick gold layer is sputtered before imaging.

SUPPLEMENTARY MATERIALS

Supplementary material for this article is available at http://advances.sciencemag.org/cgi/content/full/6/33/eaba5029/DC1

REFERENCES AND NOTES

1. F. Xia, H. Wang, D. Xiao, M. Dubey, A. Ramasubramaniam, Two-dimensional material nanophotonics. *Nat. Photonics* **8**, 899–907 (2014).
2. V. Nicolosi, M. Chhowalla, M. G. Kanatzidis, M. S. Strano, J. N. Coleman, Liquid exfoliation of layered materials. *Science* **340**, 1226419 (2013).
3. G. Hu, J. Kang, L. W. T. Ng, X. Zhu, R. C. T. Howe, C. G. Jones, M. C. Hersam, T. Hasan, Functional inks and printing of two-dimensional materials. *Chem. Soc. Rev.* **47**, 3265–3300 (2018).
4. F. Torrisi, T. Hasan, W. Wu, Z. Sun, A. Lombardo, T. S. Kulmala, G.-W. Hsieh, S. Jung, F. Bonaccorso, P. J. Paul, D. Chu, A. C. Ferrari, Inkjet-printed graphene electronics. *ACS Nano* **6**, 2992–3006 (2012).
5. A. G. Kelly, T. Hallam, C. Backes, A. Harvey, A. S. Esmaeily, I. Godwin, J. Coelho, V. Nicolosi, J. Lauth, A. Kulkarni, S. Kinge, L. D. A. Siebbeles, G. S. Duesberg, J. N. Coleman, All-printed thin-film transistors from networks of liquid-exfoliated nanosheets. *Science* **356**, 69–72 (2017).
6. D. McManus, S. Vranic, F. Withers, V. Sanchez-Romaguera, M. Macucci, H. Yang, R. Sorrentino, K. Parvez, S.-K. Son, G. Iannaccone, K. Kostarelos, G. Fiori, C. Casiraghi, Water-based and biocompatible 2D crystal inks for all-inkjet-printed heterostructures. *Nat. Nanotechnol.* **12**, 343–350 (2017).
7. R. D. Deegan, O. Bakajin, T. F. Dupont, G. Huber, S. R. Nagel, T. A. Witten, Capillary flow as the cause of ring stains from dried liquid drops. *Nature* **389**, 827–829 (1997).
8. R. G. Larson, In retrospect: Twenty years of drying droplets. *Nature* **550**, 466–467 (2017).
9. D. Mampallil, H. B. Eral, A review on suppression and utilization of the coffee-ring effect. *Adv. Colloid Interf. Sci.* **252**, 38–54 (2018).
10. H. Hu, R. G. Larson, Marangoni effect reverses coffee-ring depositions. *J. Phys. Chem. B* **110**, 7090–7094 (2006).
11. G. Hu, T. Albrow-Owen, X. Jin, A. Ali, Y. Hu, R. C. T. Howe, K. Shehzad, Z. Yang, X. Zhu, R. I. Woodward, T.-C. Wu, H. Jussila, J.-B. Wu, P. Peng, P.-H. Tan, Z. Sun, E. J. R. Kelleher, M. Zhang, Y. Xu, T. Hasan, Black phosphorus ink formulation for inkjet printing of optoelectronics and photonics. *Nat. Commun.* **8**, 278 (2017).
12. B. M. Weon, J. H. Je, Capillary force repels coffee-ring effect. *Phys. Rev. E* **82**, 15305 (2010).
13. A.-L. Biance, C. Clanet, D. Quéré, First steps in the spreading of a liquid droplet. *Phys. Rev. E* **69**, 016301 (2004).
14. L. H. Tanner, The spreading of silicone oil drops on horizontal surfaces. *J. Phys. D. Appl. Phys.* **12**, 1473–1484 (2001).
15. N. Shahidzadeh-Bonn, S. Rafaï, A. Azouni, D. Bonn, Evaporating droplets. *J. Fluid Mech.* **549**, 307–313 (2006).
16. K. S. Lee, C. Y. Cheah, R. J. Copleston, V. M. Starov, K. Sefiane, Spreading and evaporation of sessile droplets: Universal behaviour in the case of complete wetting. *Colloids Surf. A Physicochem. Eng. Asp.* **323**, 63–72 (2008).
17. A. Oron, S. H. Davis, S. G. Bankoff, Long-scale evolution of thin liquid films. *Rev. Mod. Phys.* **69**, 931–980 (1997).
18. D. Pesach, A. Marmur, Marangoni effects in the spreading of liquid mixtures on a solid. *Langmuir* **3**, 519–524 (1987).
19. G. Guéna, C. Poulard, A. M. Cazabat, Evaporating drops of alkane mixtures. *Colloids Surf. A Physicochem. Eng. Asp.* **298**, 2–11 (2007).
20. D. Brutin, V. Starov, Recent advances in droplet wetting and evaporation. *Chem. Soc. Rev.* **47**, 558–585 (2018).
21. H. Hu, R. G. Larson, Analysis of the effects of Marangoni stresses on the microflow in an evaporating sessile droplet. *Langmuir* **21**, 3972–3980 (2005).
22. P. J. Yunker, T. Still, M. A. Lohr, A. G. Yodh, Suppression of the coffee-ring effect by shape-dependent capillary interactions. *Nature* **476**, 308–311 (2011).
23. R. I. Woodward, R. C. T. Howe, G. Hu, F. Torrisi, M. Zhang, T. Hasan, E. J. R. Kelleher, Few-layer MoS_2 saturable absorbers for short-pulse laser technology: Current status and future perspectives. *Photonics Res.* **3**, A30–A42 (2015).
24. Y. Xia, R. Li, R. Chen, J. Wang, L. Xiang, 3D architectured graphene/metal oxide hybrids for gas sensors: A review. *Sensors* **18**, 1456 (2018).
25. J. Noh, M. Jung, Y. Jung, C. Yeom, M. Pyo, G. Cho, Key issues with printed flexible thin film transistors and their application in disposable RF sensors. *Proc. IEEE* **103**, 554–566 (2015).

Science Advances

A general ink formulation of 2D crystals for wafer-scale inkjet printing

Guohua Hu, Lisong Yang, Zongyin Yang, Yubo Wang, Xinxin Jin, Jie Dai, Qing Wu, Shouhu Liu, Xiaoxi Zhu, Xiaoshan Wang, Tien-Chun Wu, Richard C. T. Howe, Tom Albrow-Owen, Leonard W. T. Ng, Qing Yang, Luigi G. Occhipinti, Robert I. Woodward, Edmund J. R. Kelleher, Zhipei Sun, Xiao Huang, Meng Zhang, Colin D. Bain and Tawfique Hasan

ARTICLE TOOLS	http://advances.sciencemag.org/content/6/33/eaba5029
SUPPLEMENTARY MATERIALS	http://advances.sciencemag.org/content/suppl/2020/08/11/6.33.eaba5029.DC1
REFERENCES	This article cites 25 articles, 2 of which you can access for free http://advances.sciencemag.org/content/6/33/eaba5029#BIBL
PERMISSIONS	http://www.sciencemag.org/help/reprints-and-permissions

Use of this article is subject to the Terms of Service

Science Advances

AAAS

Supplementary Materials for

A general ink formulation of 2D crystals for wafer-scale inkjet printing

Guohua Hu, Lisong Yang, Zongyin Yang, Yubo Wang, Xinxin Jin, Jie Dai, Qing Wu, Shouhu Liu, Xiaoxi Zhu,
Xiaoshan Wang, Tien-Chun Wu, Richard C. T. Howe, Tom Albrow-Owen, Leonard W. T. Ng, Qing Yang,
Luigi G. Occhipinti, Robert I. Woodward, Edmund J. R. Kelleher, Zhipei Sun, Xiao Huang,
Meng Zhang*, Colin D. Bain*, Tawfique Hasan*

*Corresponding author. Email: mengzhang10@buaa.edu.cn (M.Z.); c.d.bain@durham.ac.uk (C.D.B.);
th270@cam.ac.uk (T.H.)

The PDF file includes:

Sections S1 to S9
Figs. S1 to S15
Table S1

Other Supplementary Material for this manuscript includes the following:

(available at advances.sciencemag.org/cgi/content/full/6/33/eaba5029/DC1)

Movies S1 to S8

Section S1. Production of 2d crystals via solution processing

Liquid-phase exfoliation (LPE) and ion intercalation: We use LPE to produce 2d crystals of graphene, transition metal dichalcogenides (TMDs: molybdenum disulfide (MoS_2), molybdenum diselenide ($MoSe_2$), and tungsten disulfide (WS_2)), hexagonal boron nitride (*h*-BN), bismuth telluride (Bi_2Te_3), indium selenide (In_2Se_3) and black phosphorus (BP). To ensure exfoliation and stable dispersions, LPE requires the use of high boiling point solvents (e.g. N-Methyl-2-pyrrolidone (NMP)) that have matched Hansen solubility parameters (*25, 26*), or solvent mixtures (e.g. water/isopropyl alcohol (IPA)) with minimized Hansen solubility parameter distance (*26*), or surfactants (e.g. sodium deoxycholate (SDC) in water) for electrostatic and/or steric stabilization (*27*).

For LPE, 100 mg bulk crystals (10 mg for BP) are mixed with 10 mL NMP (anhydrous NMP for BP), water/IPA (55 vol.%/45 vol.%) or water/SDC (SDC concentration 7 gL^{-1}). The bulk graphite, TMDs, *h*-BN, Bi_2Te_3 and In_2Se_3 are purchased from Sigma. The bulk BP is purchased from Smart-Elements. The mixtures are sonicated in a 20 kHz bath sonicator for 12 hours at 15°C, and then centrifuged at 4,000 rpm for 1 hour. The upper 70% of the resultant dispersions are collected for inkjet printing and spray coating without further ink formulation following previous reports, as well as ink formulation through solvent exchange (see Section S4).

As will be discussed in Section S4, certain 2d crystals (for instance *h*-BN and In_2Se_3) produced by this method may not formulate dispersions with sufficient stability for inkjet printing. Therefore, in addition to LPE, we also use ion intercalation assisted exfoliation to produce *h*-BN, In_2Se_3 and MoS_2, following the methods reported in Refs. (*28, 29*). For this, 1 g bulk crystals of MoS_2, In_2Se_3 and *h*-BN are mixed into 30 mL of water and 1 mL hydrazine hydrate (Sigma), followed by 30 min bath sonication. The mixtures are then transferred into autoclaves and heated at 120°C for 8 hours. The treated MoS_2, *h*-BN and In_2Se_3 are washed and dried, and then mixed into 3 mL 1.6 M butyllithium solution in hexane (Sigma-Aldrich) for 48 hours. The resultant MoS_2, *h*-BN and In_2Se_3 are washed with hexane (60 mL) and dispersed in water via 1 hour bath sonication. The exfoliated MoS_2, *h*-BN and In_2Se_3 are next washed with water for three times. The washed MoS_2 is dispersed in 20 mL water and sonicated for 1 hour, followed by 1 hour centrifugation at 4,000 rpm. The upper 70% of the resultant dispersion is collected for ink formulation (see Section S4). To differentiate between the MoS_2 produced via LPE and ion intercalation, they are named as 2H-MoS_2 and 1T-MoS_2, respectively (*28, 29*). The washed *h*-BN and In_2Se_3 are dispersed in 20 mL water/IPA (55 vol.%/45 vol.%) and sonicated for 1 hour, followed by 30 min centrifugation at 1,000 rpm. The upper 70% of the resultant dispersions are collected for ink formulation (see Section S4).

Chemical synthesis: The 2d crystals of tin disulfide (SnS_2) and $Sn_{0.5}W_{0.5}S_2/SnS_2$ heterostructure are produced via chemical synthesis, following the method reported in Ref. (*30*). In a typical synthesis process of SnS_2, 0.25 mmol $SnCl_4 \cdot 5H_2O$ (Sigma) and 3.75 mmol $CS(NH_2)_2$ (J&K chemical, Shanghai) are dissolved in 19.45 mL water and stirred for 2 hours. This solution is then transferred to an autoclave, and heated at 220°C for 12 hours. The obtained product is then centrifuged at 8,000 rpm for 10 min. The obtained precipitate is washed with water for three times for ink formulation (see Section S4). In a typical synthesis process of $Sn_{0.5}W_{0.5}S_2/SnS_2$, 0.25 mmol $(NH_4)_{10}H_2(W_2O_7)_6$, 7.5 mmol $CS(NH_2)_2$, and 0.5-0.625 mmol $SnCl_4 \cdot 5H_2O$ are dissolved in 19.45 mL water and stirred at 80°C for 2 hours. This solution is then transferred to an autoclave, and heated at 220°C for 60 hours. The obtained product is then centrifuged at 8,000 rpm for 10 min. The precipitate is then washed with water for three times for ink formulation (see Section S4). We

show in Fig. S2a-d SEM and TEM micrographs of the SnS_2 and $Sn_{0.5}W_{0.5}S_2/SnS_2$ samples. In particular, Fig. S2c,d show that the $Sn_{0.5}W_{0.5}S_2$ nanoplates have been successfully grown on SnS_2.

Hydrothermal synthesis: The graphene hybrid, i.e. reduced graphene oxide decorated with spindle-like α-Fe_2O_3 (rGO/α-Fe_2O_3) is produced via hydrothermal synthesis. In a typical process, 5.6 mg graphene oxide monolayer flakes (99% of the flakes are monolayers; Tanyuanhuigu, Shanghai) are dispersed in 11.25 mL water, followed by 30 min bath sonication. The GO dispersion is mixed with an $FeCl_3$ (Sigma) solution (36.5 mg in 9 mL water), and added with another 13.5 mL IPA and 180 mg CH_3COONa. The resultant mixture is sonicated for 30 min, transferred to an autoclave and heated at 120°C for 8 hours. The produced rGO/α-Fe_2O_3 is washed with water for three times for ink formulation (see Section S4).

Material characterizations: We characterize the thickness and lateral dimension of the produced 2d crystals used in inkjet printing demonstrations; Fig. S1. These include 2H-MoS_2, WS_2, $MoSe_2$ and BP produced via LPE, 1T-MoS_2, h-BN and In_2Se_3 produced via ion intercalation, $Sn_{0.5}W_{0.5}S_2/SnS_2$ and SnS_2 produced via chemical synthesis, and rGO/α-Fe_2O_3 produced via hydrothermal synthesis. The thickness and lateral dimension are typically acquired by AFM, except the thickness histograms of the $Sn_{0.5}W_{0.5}S_2/SnS_2$ and SnS_2 that are acquired through SEM. Since the SnS_2, $Sn_{0.5}W_{0.5}S_2/SnS_2$ and rGO/α-Fe_2O_3 are not produced via typical top-down exfoliation techniques, they are also characterized with SEM and TEM; Fig. S2. The AFM samples are characterized with a Bruker Dimension Icon AFM in ScanAsyst™ mode, using a silicon cantilever with a silicon nitride tip. The SEM samples are characterized with JEOL JSM-7800F. The TEM samples are characterized with JEOL 2100Plus.
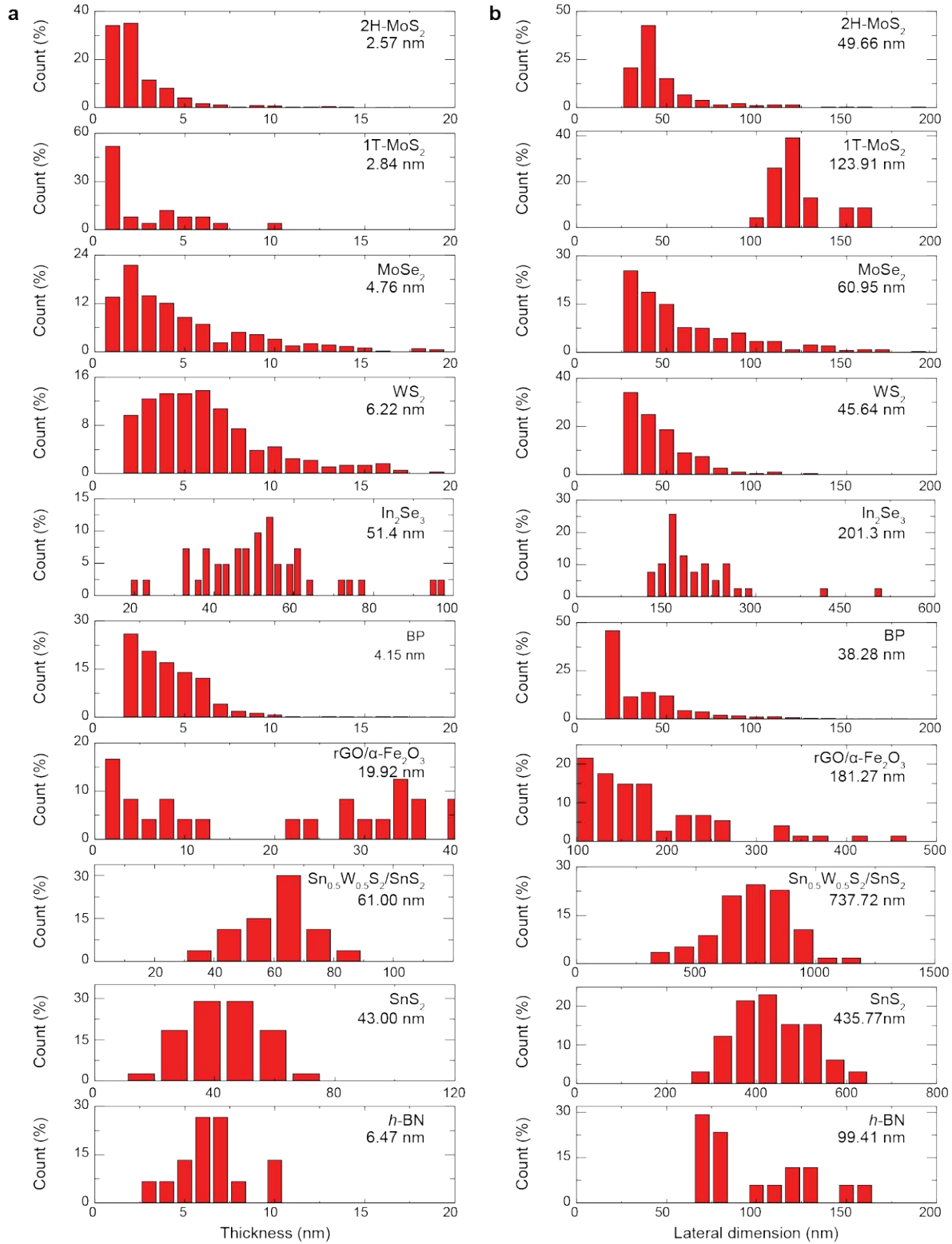
Fig. S1. Characterization of the produced 2d crystals. Distribution of (a) thickness and (b) lateral dimension of the 2d crystals, with the average values presented.
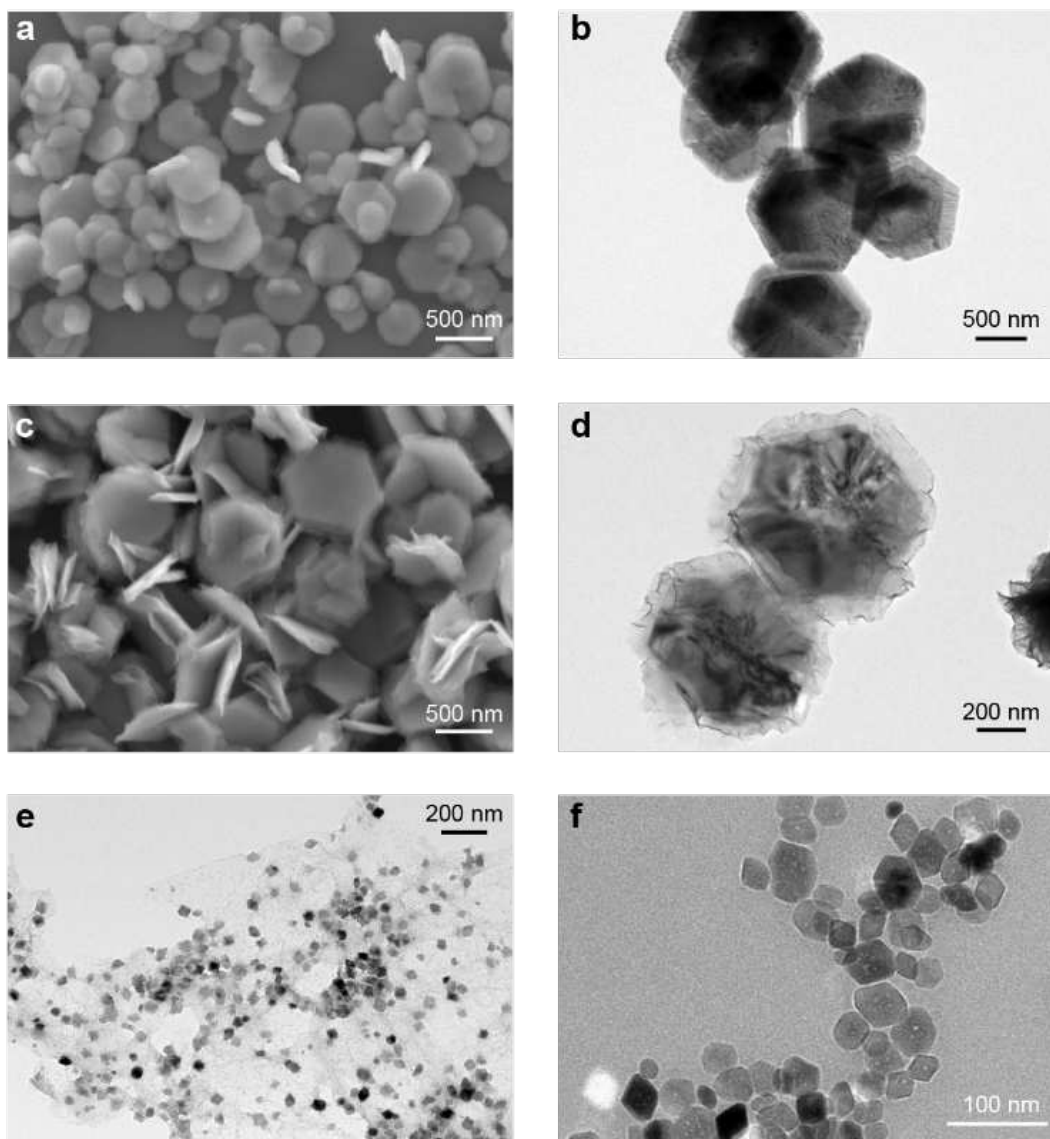
Fig. S2. Characterization of the synthesized 2d crystals. (a) SEM and (b) TEM micrographs of typical SnS_2 2d crystals; (c) SEM and (d) TEM micrographs of typical $Sn_{0.5}W_{0.5}S_2/SnS_2$ flakes, showing $Sn_{0.5}W_{0.5}S_2$ nanoplates are grown on the SnS_2 flakes. (e,f) TEM micrographs of rGO/α-Fe_2O_3, showing the α-Fe_2O_3 nanoparticles are grown on the rGO flakes.

Section S2. Inkjet printing and spray coating of the solution-processed dispersions

LPE dispersions of 2d crystals have been commonly adapted to inkjet printing without further ink formulations (3–6). These include the dispersions in organic solvents (e.g. NMP), solvent mixtures (e.g. water/IPA), and water with surfactants (e.g. water/SDC) (3, 31).

In Table S1, we show the inverse *Ohnesorge* numbers (Z) of these LPE dispersions and the common solvents used. Generally, the Z value of an ink is used to determine whether it would form a stable jetting of individual droplets under each electrical drive pulse: $Z = \sqrt{\gamma \rho a}/\eta$, depending on the viscosity (η), surface tension (γ), and density (ρ), and the inkjet cartridge nozzle diameter (a) (4). An established guiding principle is that Z should be 1-14 to avoid the formation of satellite droplets (>14) or elongated ligaments (<1) during the jetting process.

As shown in Table S1, Z values of the NMP and water/SDC based LPE dispersions are >15, while the value for water/IPA based dispersions approach 14. This indicates that these LPE dispersions tend to generate satellite droplets (4, 32). Indeed, jetting of such satellite droplets is observed with NMP based dispersions; Fig. S3a. This can even lead to jetting deviations from the jetting path, as shown in Fig. S3b, causing the droplets to deposit on untargeted areas. As a result, printing using these dispersions can lead to nonuniformity, as demonstrated in Fig. S3c,d where the typical morphologies with one single and multiple print repetitions on Si/SiO$_2$ are presented. In addition to unstable jetting, heavy coffee rings are also formed with these dispersions at the edges of each of these single and overlapped droplets.

Meanwhile, as shown in Fig. S3c,d, inkjet printing with these LPE dispersions also cannot appropriately wet the Si/SiO$_2$ substrate for a continuous feature with either single or multiple print repetitions. Under such wetting conditions, the droplets would nonuniformly retract during drying, resulting in poor uniformity. To allow appropriate wetting for a consistent deposit, the ink surface tension should be 7-10 mNm^{-1} lower than the substrate surface energy; otherwise, the deposited droplets retract and ball-up during drying (33). With such high surface tensions of >32 mNm^{-1}, these dispersions therefore cannot wet the substrates commonly used in electronics and optoelectronics, including Si/SiO$_2$ and glass (36 mNm^{-1}) (34) and plastics such as PET (48 mNm^{-1}) (35). A commonly adopted solution to enhance wetting is to increase the substrate surface energy via surface treatments, e.g. by oxygen plasma. Alternatively, lowering the surface tension of the inks by adding e.g. low-surface tension solvents such as alcohols or additive surfactants and polymers is also viable and widely adopted. However, the use of additives could be detrimental as they disrupt formation of an electrically continuous network between individual nanostructures. In this work, we focus on additive-free ink formulation using a mixed alcohol carrier, with a surface tension of <30 mNm^{-1} for wetting of a wide range of substrates without the need for surface treatments. We note that spray coating with these NMP, water/SDC and water/IPA based dispersions on PET also fails to develop a continuous deposited feature; Fig. S3e,f. In this case, 0.5 mL dispersions are sprayed at room temperature.

As shown in Table S1, alcohols (e.g. IPA and the butanols) tend to give Z values within the 1-14 range, suggesting that these alcohols are suitable solvents for inkjet ink formulation. Indeed, alcohols such as IPA have been widely used in graphics (36) and recent 2d crystal ink formulations (3, 31). Also, their low surface tensions (<30 mNm^{-1}) tend to ensure adequate wetting of the substrates. However, as demonstrated in Fig. 1d and as will be seen in Movie S5, pure alcohols do not suppress the CRE, and leads to nonuniform deposits.

Table S1. Physical properties and the Z values for some common solvents and the 2d crystal dispersions and the formulated inks. The temperature is 20°C unless otherwise stated. The vapor pressure (P_V) is calculated by Antoine equation ($\lg P_V = A + B/T + C\lg T + DT + ET^2$), where T is the absolute temperature in K and P_V is in mmHg in the equation and converted to kPa in the table. The Antoine parameters, A, B, C, D and E are taken from Ref. (*37*). Pendant droplet measurement and parallel plate rheometer are used to measure the surface tension and the viscosity of the LPE dispersions and the formulated inks, respectively. The nozzle diameter of the Dimatix DMC-11610 cartridge, a, is 22 µm.

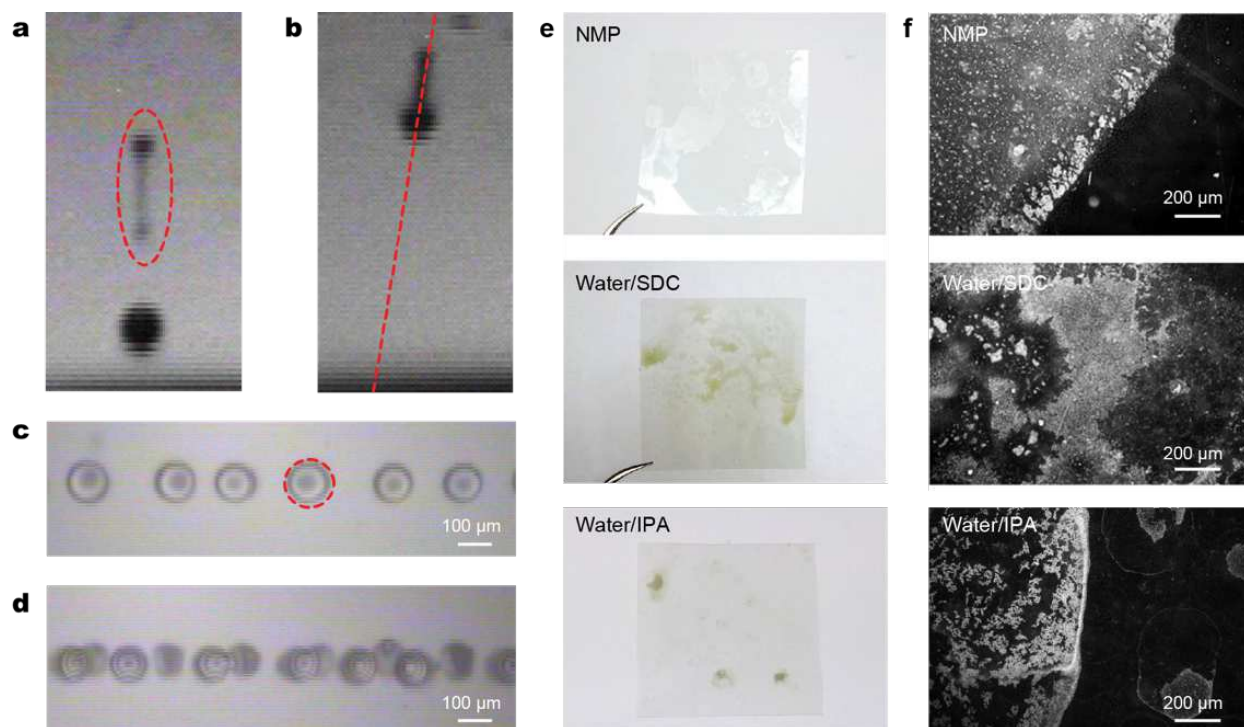|	P_V (kPa)	γ (mNm^{-1})	η (mPas)	ρ (gcm^{-3})	$Z = \dfrac{\sqrt{\gamma\rho a}}{\eta}$
Common solvents					
NMP		40.7 (*38*)	1.7 (*38*)	1.0 (*38*)	18
Water		72.9 (*39*)	1.0 (*40*)	1.0 (*41*)	40
Ethanol	5.8	22.4 (*39*)	1.2 (*38*)	0.8 (*41*)	17
IPA	4.4	21.3 (*39*)	2.4 (*38*)	0.8 (*38*)	8
2-butanol	1.7	22.9 (*39*)	3.8 (*38*)	0.8 (*38*)	5
t-butanol	4.0	20.7 (*42*)	4.3 (25°C) (*43*)	0.8 (25°C) (*43*)	4
LPE dispersions					
NMP based		42	2.0	1	15
Water/IPA based		32	2.0	0.9	13
Water/SDC based		45	0.8	1	39
IPA/2-butanol (10 vol.%) inks		28	2.2	0.8	10

Fig. S3. Inkjet printing with the solution-processed dispersions. Typical micrographs for the generation of (a) satellite droplet as indicated by the dashed circle, and (b) jetting deviation from the intended vertical patch, as indicated by the dashed line, observed through the inkjet printer stroboscopic camera. Typical micrographs for printing morphologies with (c) one single print repetition and (d) multiple print repetitions on Si/SiO$_2$, showing coffee rings and poor-wetting; the red circle in (c) indicates a coffee-ring. (e) Photographs of sprayed films (3 × 3 cm) on PET and (f) corresponding optical dark-field micrographs. Demonstrated with 2H-MoS$_2$ LPE dispersions. Photo Credit: Guohua Hu, University of Cambridge and The Chinese University of Hong Kong.

Section S3. Solutal Marangoni effect of the mixed solvent ink formulation

Supplementary Movies

Drying sessile droplets with tracer particles

Movie S1: The flows of a drying pL-droplet from IPA with the tracer particles by dark-field imaging. Drop drying time $t_f = 178$ ms.

Movie S2: The flows of a drying pL-droplet from IPA/ethanol (10 vol.%) with the tracer particles by dark-field imaging. Drop drying time $t_f = 201$ ms.

Movie S3: The flows of a drying pL-droplet from IPA/2-butanol (10 vol.%) with the tracer particles by dark-field imaging. Drop drying time $t_f = 138$ ms.

Movie S4: The flows of a drying pL-droplet from IPA/t-butanol (10 vol.%) with the tracer particles by dark-field imaging. Drop drying time $t_f = 125$ ms.

Movie S5: The flows of a drying pL-droplet from 2-butanol with the tracer particles by dark-field imaging. Drop drying time $t_f = 444$ ms. This is a controlled experiment to demonstrate that 2-butanol cannot suppress the CRE.

Drying sessile droplets without tracer particles

Movie S6: Spreading and drying of a pL-droplet from IPA/2-butanol (10 vol.%) by film interferometry. Drop drying time $t_f = 148$ ms. The Movie is used for droplet profile reconstruction in Fig. 2e at 0.13 t_f, 0.33 t_f, 0.53 t_f, 0.73 t_f and 0.93 t_f.

Movie S7: Spreading and drying of a pL-droplet from IPA/ethanol (10 vol.%) by film interferometry. Drop drying time $t_f = 150$ ms.

Movie S8: Spreading and drying of a pL-droplet from IPA/2-butanol (10 vol.%) by shadow imaging in synchronization with Movie S6. The Movie is used for droplet profile reconstruction in Fig. 2e at 0.004 t_f.

Note that the respective drying time for the IPA and IPA/t-butanol (10 vol.%) droplets without tracer particles is 188 ms and 174 ms.

Scale bars in the movies (Supplementary Movie S1-S8) are 40 µm.

Materials

The solvents used in the experiments are as follows: IPA (Fisher scientific, Laboratory reagent grade), ethanol (Fisher scientific, analytical regent), 2-butanol (Sigma-Aldrich, Reagent 99%), and t-butanol (Alfa Aesar, ACS reagent grade 99%+). PVP- stabilized [poly(N-vinylpyrrolidone)] PS (polystyrene) particles (755 nm) (preparation in Ref. (*44*)) are used as the tracer particles in all experiments. Dry PVP-PS particles are weighed to make suspension in a range of 0.04-0.06 wt.% through 30 min bath sonication. The suspensions exhibit no obvious sedimentation over a day. Microscopic glass coverslip (Academy Science, 0.13-0.17 mm thickness) is cleaned by acetone/ ultrapure water/IPA/N_2 stream.

Experimental methods

Droplets of a typical volume of 40-50 pL are dispensed onto the glass coverslip from a drop-on-demand device (MJ-ABP-01, MicroFab Technologies, nozzle diameter 30 µm) under a bipolar waveform through a MicroFab device (JetDrive III controller CT-M3-02). The set-ups for the

study of the flows of a drying droplet and the film formation have been presented elsewhere (*45*, *46*). In brief, in the flow setup, the sample is illuminated by a light-emitting diode (505 nm, Thorlabs) from an angle so that only scattered light from particles can be collected by the objective lens (50x/0.6, Nikon) underneath the substrate and hence, dark-field image is obtained. The flow is recorded by a high-speed camera (APX-RS, Photron). For film interferometric imaging, another light-emitting diode light (505 nm, Thorlabs) is used to illuminate the sample underneath the substrate. The reflected light from the interfaces of liquid-air and liquid-solid interferes and fringes can be observed when the thickness of the film is less than the coherent length of the light source, where the fringe contrast is also limited by reflectance of two interfaces of the droplet. Two neighboring bright or dark fringes have a thickness difference of $\lambda/(2n')$, where λ is the light wavelength and n' is the refractive index of the liquid sample, i.e. approximately 180 nm in our experimental condition. Both the image views can be switched on at the same time though a separate view that gives a better image contrast. A shadow view from the side of the sessile droplet is also utilized for the determination of initial droplet volume and the contact angle at the early stage of spreading via an objective lens (20x/0.42, Edmund Optics) and a high-speed camera (CR450x3, Optronis). Cameras and MicroFab controller are synchronized from the same trigger. The imaging system is calibrated by a micro calibration plate (Lavision), giving a resolution of 0.35 μm/pixel for the view from underneath and 0.58 μm/pixel from side, respectively. All the experiments are carried out at room temperature of $21 \pm 1°C$ and relative humidity of $45 \pm 5\%$ (note that in moist air, water may condense into the drying alcohol droplets and affect their spreading dynamics). The particles are traced, and the speed is calculated over time and region binning with a custom-written Matlab code adapted from Ref. (*47*). The contact line of the spreading film is traced and analyzed as a function of time, and the droplet shape is reconstructed from interference fringes when droplet spreads and thins to a thickness of less than 3 μm.

Discussion of thermal and solutal Marangoni effect

Typically, compositional surface tension gradients are orders of magnitude larger than the thermal ones at ambient conditions (*21*). Chen *et al.* recently investigated the Marangoni effects on the drying of a pure solvent and binary solvent mixtures on a hydrophobic substrate with a heat control from 22-80°C (*48*). They showed that for a pure water droplet the thermal Marangoni effect appears only when the substrate is heated to >50°C. The pure 1-butanol droplet (less volatile than water) does not show any thermal instability at any heated temperature. However, 5% 1-butanol/water mixture shows solutal Marangoni effect at any substrate temperate. Jambon-Puillet *et al.* also studied very recently the spreading dynamics of sessile droplets of alkenes with the vapor pressure varied over two orders of magnitude (from nonane of 0.59 kPa to pentane of 53 kPa) (*49*). They showed a good agreement in droplet spreading for heptane (vapor pressure of 4.6 kPa) and the other less volatile alkenes where the thermal effect is neglected in their spreading model. This again infers that the thermal effect is trivial for medium volatile solvents.

We have shown in the manuscript that IPA, IPA/ethanol and IPA/*t*-butanol droplets without tracer particles have almost identical behavior that falls onto theoretical 'universal curves' for the case of complete wetting of a pure fluid in the absence of thermal Marangoni effects (*16*). Their spreading curves at (0.01-0.03) t_f (Fig. 2d) are fitted with power law exponents close to the predicted values under a simple model of sessile droplet subject to capillary and viscous forces. Here we replot Fig. 2d as Fig. S4a. In their evaporation phase during (0.68-0.97) t_f, a fit in $D \approx (1-t/t_f)^n$ gives us n as 0.52 for IPA, 0.53 for IPA/ethanol, and 0.51 for IPA/*t*-butanol. These slopes lie between the value of 0.50 (the 'D^2 law') predicted from a diffusive model with a constant contact

angle (*15*) and the value of 0.54 predicted in a recent analysis by Saxton *et al.* (*50*). These exponents are slightly higher than the values obtained from microliter drops of pure alkanes reported in the range of 0.42-0.49 (*51, 52*). The results suggest that there is no obvious sign of thermal Marangoni flows in these three cases and that coffee rings are formed in a similar manner.

On the contrary, IPA/2-butanol has enhanced spreading (Fig. 2d), where the mixed solvent droplet spreads outwards for 60% of the drying time, preventing the formation of a deposit at the contact line. We note that the enhanced spreading also occurs in the experiments described above where the droplet contains tracer particles. The presence of these tracer particles reduces the duration of the spreading phase from 0.6 t_f (without particles) to 0.36 t_f (with tracer particles). The spreading and drying are strongly coupled and leads to a complex drying curve (Fig. S4a) with a simple power law fit only at final stage of drying (0.89-0.97) t_f, where we get an exponent of 0.62.

We have shown in Fig. 2e that the droplet shape of IPA/2-butanol without tracer particles is transformed dramatically from a spherical-cap shape to a 'pancake' shape as early as 0.33 t_f. The internal flow reduces speed greatly around (0.40-0.45) t_f (Fig. 2b,c). Note that the droplet height profile at 0.004 t_f is reconstructed from side-view shadow image, while the others are reconstructed interferometric profiles. For dynamics, refer to Movie S6 and S8. In Fig. S4b, we compare interference microscopy images of IPA/ethanol and IPA/2-butanol droplets without tracer particles around halfway through drying (0.45 t_f). As shown, the IPA/ethanol droplet is an almost perfect spherical-cap despite the presence of a Marangoni stress along the free surface acting from the contact line towards the apex: capillarity dominates the shape. In contrast, the IPA/2-butanol droplet (which is still spreading outwards at 0.45 t_f) has a 'pancake' profile with an approximately uniform thickness of 1 μm over the contact diameter of ~200 μm before curving to meet the substrate with a contact angle of ~3°.

We attribute the unique spreading and evaporation behavior of IPA/2-butanol to a solutal Marangoni effect. The surface tension difference needed to drive this flow in the IPA/2-butanol can be estimated from the increase in radial velocity of particles at early times (when the droplet shapes are the same) compared to the pure IPA (Fig. 2b,c). As we compare the flow velocities between IPA/2-butanol and IPA at (0.1-0.15) t_f, the particle speed is almost doubled in the former case. We attribute the extra value of ~0.2 mm s^{-1} (near the contact line) to be Marangoni stress induced. The tangential component of viscous stress is balanced by the stress associated with surface tension gradients, i.e. $d\gamma = \eta(u/h)R \sim 10^{-5}$ Nm^{-1}, where γ is the surface tension, η is the viscosity, u is the Marangoni flow speed of 0.2 mm s^{-1}, h is the droplet height of ~1 μm at 1/3 of the drying time, and R is the contact radius of 80 μm. That is to say that the surface tension difference between the contact line and the apex is $O(10^{-5}$ Nm$^{-1})$ compared to a surface tension difference between the two pure solvents of $O(10^{-3}$ Nm$^{-1})$.

The average evaporation rate of a sessile droplet from a pure fluid can be estimated by (*53*):

$$-\dot{m} \approx \pi R D_V \rho_V (0.27\theta^2 + 1.30) \approx 4 R D_V \rho_V \qquad (1)$$

where R is the droplet contact radius, D_V is the diffusion coefficient of the vapor, $\rho_V = M_W P_V/(R_{gasconstant} T)$ is the vapor density via the ideal gas law, $R_{gasconstant} = 8.3$ Jmol^{-1}K^{-1} is the gas constant, T is absolute temperature in K, M_W is the molecular weight, and P_V is the vapor pressure. Note θ is ≤ 1 in our pinned case. Our droplet initial volume is 40-50 pL (say 45 pL) and R is 80 μm for the pinned cases. The diffusion coefficient is 1.18 ×, 0.993 ×, 0.880 × and 0.873 × 10^{-5} m^{2}s^{-1} for ethanol, IPA, 2-butanol and *t*-butanol, respectively (*54*). The average evaporation rate is 4.1 ×, 3.4 ×, 1.4 × and 3.4 × 10^{-10} kgs^{-1} for ethanol, IPA, 2-butanol and *t*-butanol, respectively.

IPA therefore evaporates about 2.4 times as fast as 2-butnaol and will be depleted first at the contact line as the vapor flux is the highest at the contact line. The enhanced spreading in IPA/2-butanol strongly indicates that the preferential evaporation of IPA (the lower surface tension component) has created a surface tension gradient at the droplet surface. This Marangoni stress leads a flow established from the droplet apex to the contact line. The nanoparticle-enriched zone at the (moving) contact line is constantly overtaken by fresh solution from the centre, maintaining a uniform concentration profile. IPA and t-butanol have almost the same evaporation rates. It is therefore understandable that their mixture will behave like pure IPA. Ethanol evaporates slightly faster than IPA, which may lead to Marangoni flows opposite to the outward capillary flow. However, the suppression of spreading or acceleration of the contact line retraction has not been observed. This indicates that the flows are still capillarity dominated and the coffee-ring deposit therefore forms similarly as IPA and IPA/t-butanol. The surface tension of the 90% IPA / 10% co-alcohol mixtures is close to that of IPA – for an ideal mixture it will be $\sigma_{IPA} + 0.1\ \Delta\sigma$, where $\Delta\sigma$ is the difference in surface tensions between the pure co-alcohol and IPA. For IPA/ethanol, the ethanol evaporates faster than the IPA so the surface tension near the contact line moves towards the value for pure IPA. The maximum difference in the surface tension between the apex and the contact line is therefore $0.1\ \Delta\sigma$. For IPA/2-butanol, the IPA evaporates faster and so the liquid near the contact line is enriched in 2-butanol. The maximum surface tension at the contact line is $\sigma_{2\text{-butanol}}$. Hence the maximum surface tension difference between the contact line and the apex is $0.9\ \Delta\sigma$. Consequently, much larger Marangoni stresses can arise in the 9:1 IPA/2-butanol mixture than in the 9:1 IPA/ethanol mixture.
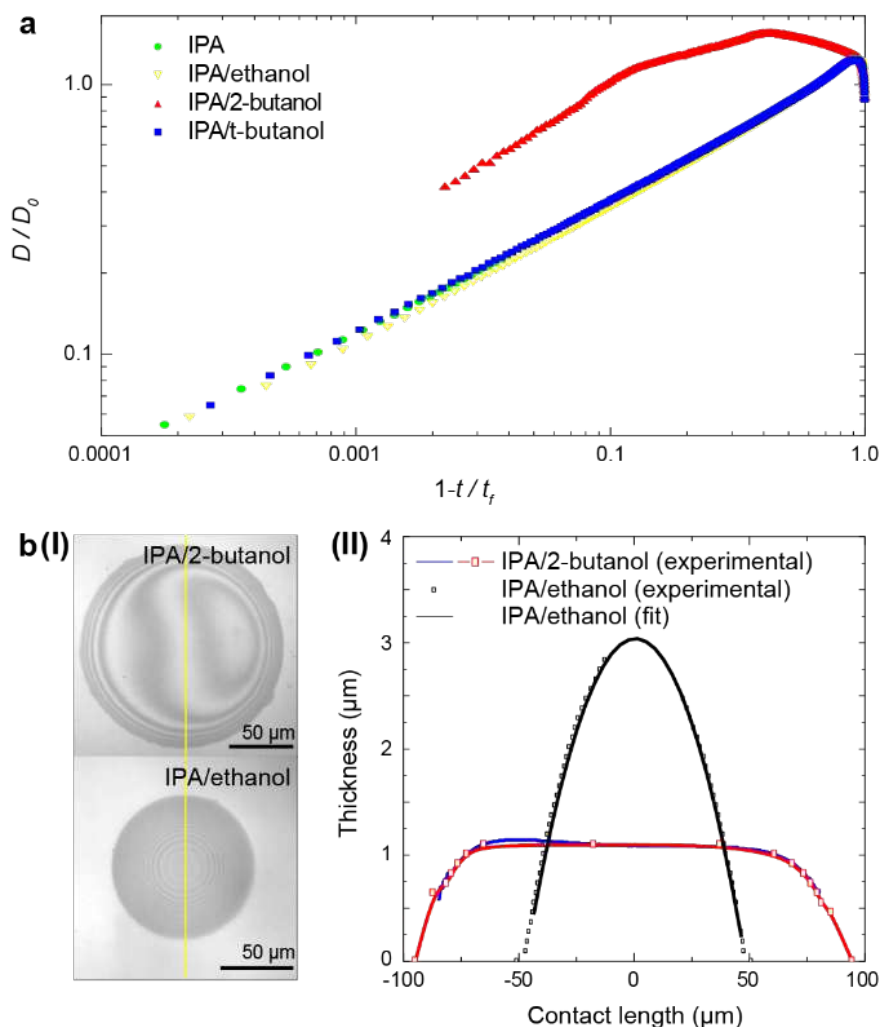
Fig. S4. Contact diameter of spreading droplets and droplet shape profiles. (a) Normalized contact diameter of a drying droplet as a function of normalized remaining drying time for IPA and the IPA-based alcohol binaries. Replotted from Fig. 2d. (b) Interference studies of drying IPA/2-butanol and IPA/ethanol droplets without tracer particles at $t = 0.45$ t_f: (I) interference micrographs; (II) the reconstructed droplet shape profiles, open squares with *B-spline* line is from cross section of the frame, and blue line is reconstructed from tracing frames near the center of the drop; for IPA/ethanol, open squares is from cross section of the frame, and black line is circle fit. For dynamics, refer to Movie S6 and S7.

Section S4. Formulation and printing of mixed solvent inks

IPA/2-butanol (10 vol.%) inks:

The 2d crystal flakes in the LPE dispersions are extracted through vacuum filtration. These 2d crystals include graphene, BP, h-BN, TMDs (2H-MoS$_2$, MoSe$_2$, WS$_2$), Bi$_2$Te$_3$, and In$_2$Se$_3$. Note the flakes extracted from water/SDC are repeatedly washed with water to remove the residual SDC. For ink formulation, these obtained 2d crystals are dispersed in IPA/2-butanol (10 vol.%) through 10 min bath sonication. These inks differ in stability against sedimentation: the graphene, h-BN, In$_2$Se$_3$ and Bi$_2$Te$_3$ inks remain stable for a few hours, insufficient for long-term inkjet printing processes. However, the TMD inks and the BP ink are stable without visible aggregations for up to weeks, sufficient for large-scale inkjet printing.

Since 1T-MoS$_2$ requires water to remain stable for long-term printing, the obtained water-based 1T-MoS$_2$ dispersion is diluted with IPA/2-butanol (10 vol.%) by 10 times for ink formulation. The h-BN and In$_2$Se$_3$ produced via ion intercalation are extracted by vacuum filtration, and then redispersed in IPA/2-butanol (10 vol.%) through 10 min bath sonication for ink formulation.

The washed SnS$_2$, Sn$_{0.5}$W$_{0.5}$S$_2$/SnS$_2$ and rGO/α-Fe$_2$O$_3$ are redispersed in IPA/2-butanol (10 vol.%) through 10 min bath sonication for ink formulation.

Ink formulation strategy:

We start ink formulation from pure IPA. Short-chain alcohols, such as IPA, are widely used in graphics inks (*36*) and recently, in 2d crystal inkjet printable inks (*3*). They present appropriate fluidic properties for satellite-free inkjet printing (Table S1). The low surface tension of IPA also ensures good wetting of high-energy substrates. However, as shown in Fig. 1d, the contact line of pure IPA based inks still pins and CRE persists.

Having demonstrated the limitation with pure IPA, we investigate binary solvent systems, with IPA as the primary solvent. To induce variable Marangoni effects, we choose mixtures of IPA with additional 10 vol.% of ethanol, 2-butanol and t-butanol (secondary solvents) for ink formulation. These alcohol combinations are all zeotropic and show only small deviations from ideality. We have listed the surface tensions (γ) and vapour pressures of the alcohols in Table S1. As we have discussed in the manuscript, we expect that the radial surface tension gradient, dγ/dr, of IPA/ethanol to be <0; >0 for IPA/2-butanol; ≈0 for IPA/t-butanol. Figure 1f shows that only IPA/2-butanol suppresses the coffee-ring effect, yielding an even distribution of flakes across the deposit. However, the other mixtures show ring stains. We then conduct further careful investigation on the Marangoni effect in the IPA/2-butanol inks, as presented in the Manuscript.

To experimentally find an appropriate solvent volume ratio for the IPA/2-butanol formulation, we investigate other volume percentages of 2-butanol. Fig. 1g shows the optical micrograph of IPA/2-butanol (20 vol.%). Similar to the 10 vol.% case, the 20 vol.% droplet does not show significant coffee rings, suggesting the coffee-ring effect is also suppressed in this case. However, as we can observe, the 20 vol% droplet shows fuzzier edges and more condensed materials at the edges, as compared to the 10 vol.% droplet. Its diameter is also increased to ~74 μm (~68 μm for 10 vol.%). An increased diameter is not ideal for functional printing as it means a decreased printing resolution in device fabrication. Meanwhile, we observe the 20 vol.% droplet dries slower as more 2-butanol takes a longer time to evaporate. We note that a larger volume (>20 vol.%) of 2-butanol leads to a weaker suppression of the coffee-ring effect, fuzzier edges, larger diameter and also a longer drying time. Based on the above considerations, we chose 10 vol.% for the ink formulation.

We note that besides the IPA/2-butanol (10 vol.%) ink formulation, other alcohol mixtures fitting this solutal Marangoni mechanism are also proven viable, for instance IPA/1-propanol (10 vol.%) and IPA/1-butanol (10 vol.%).

Fig. S5. Photograph of the formulated inks in this work. This includes graphene, BP, TMDs (2H-MoS_2, $MoSe_2$, WS_2) and Bi_2Te_3 produced via LPE, h-BN, 1T-MoS_2 and In_2Se_3 produced via ion intercalation, SnS_2 and $Sn_{0.5}W_{0.5}S_2$/SnS_2 produced via chemical synthesis, and rGO/α-Fe_2O_3 produced via hydrothermal synthesis. Typical ink concentration is ~1 gL^{-1}. Photo Credit: Guohua Hu, University of Cambridge and The Chinese University of Hong Kong.
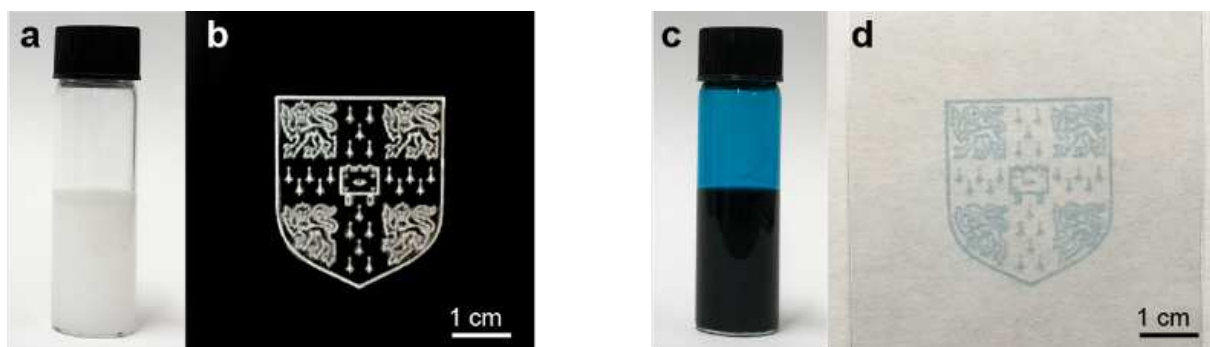

Fig. S6. Inkjet printing of nanoparticle and organic material inks. Inkjet printing of (a,b) nanoparticles and (c,d) organics on PET using the ink formulation of IPA/2-butanol (10 vol.%) solvent composition. Polystyrene nanobeads are used as the nanoparticle example. For ink formulation, polystyrene nanobeads solution (800 nm, 10 wt.%; Sigma) is diluted with IPA/2-butanol (10 vol.%) by 50 times. N,N,N',N'-Tetramethyl-4,4'-diaminotriphenylcarbenium oxalate (Sigma) is used as the organic material example. For ink formulation, it is dissolved in IPA/2-butanol (10 vol.%) at 5 gL^{-1} concentration. Photo Credit: Guohua Hu, University of Cambridge and The Chinese University of Hong Kong.

Section S5. Spray coating of the formulated inks

The formulated inks have a viscosity of 2.2 mPas, indicating that the inks can be used with low viscosity dispersion deposition techniques, for instance, spray coating and inkjet printing (*4, 32, 55*). Note as discussed, the surface tension of the inks (~28 mNm^{-1}) ensures that the inks wet common substrates including such as Si/SiO$_2$, glass and PET for a consistent deposit.

Fig. S7a presents a sprayed 2H-MoS$_2$ film. In this case, 0.5 mL 2H-MoS$_2$ ink is sprayed onto PET at room temperature. SEM characterization of the sprayed 2H-MoS$_2$ film further demonstrates even flake distributions without discernible pinholes; Fig. S7b,c. Note that the sprayed 2H-MoS$_2$ PET film is sputtered with 6 nm thick gold for SEM characterization. We also measure spatial optical absorbance of the sprayed 2H-MoS$_2$ film at 550 nm with 1 cm step interval using UV-Vis spectroscopy. The acquired spatial absorbance (after subtraction of substrate absorbance) is 0.0448 ± 0.0019; Fig. S7d. This small standard deviation, 4.2%, in spatial absorbance demonstrates that the inks allow highly spatially consistent large-area coating. Fig. S7e presents the absorbance of 2H-MoS$_2$ films sprayed with varied ink volumes. The absorbance linearly scales with the ink volume: 0.0899 per mL, with a 2.1% standard deviation. This shows that the inks allow a good controllability over the optical densities of the deposited films.

The inks with insufficient stability for long-term inkjet printing can be suitably deposited with spray coating. Besides 2H-MoS$_2$, we also show in Fig. S7a sprayed films of graphene and In$_2$Se$_3$ (exfoliated via LPE). As shown, the sprayed films are visually uniform. Indeed, the respective measured spatial optical absorbance is 0.31533 ± 0.002 and 0.47256 ± 0.002, demonstrating standard deviations <1%. 5 mL inks are sprayed.
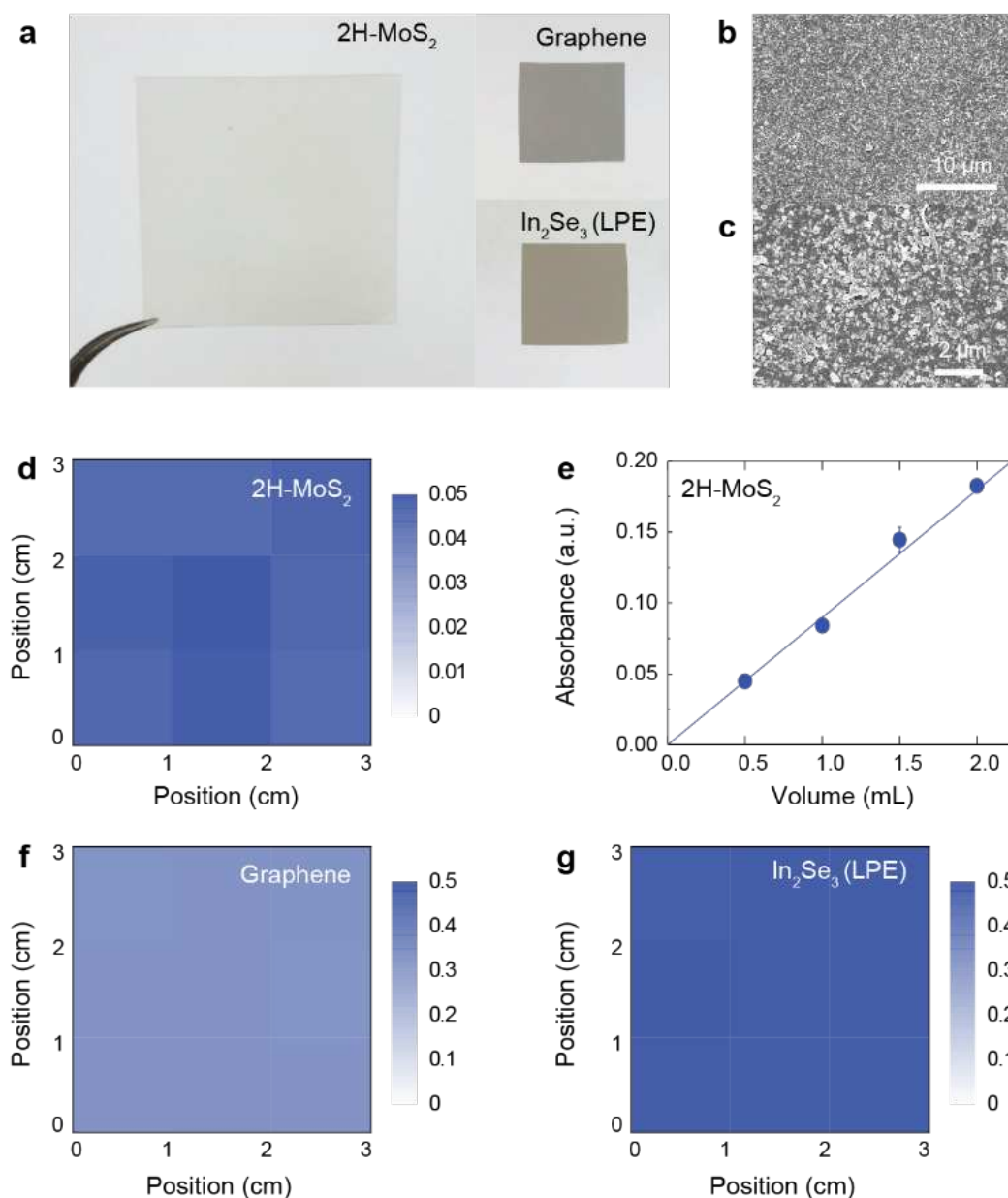
Fig. S7. Spray coating with the formulated inks in this work. (a) Photographs of sprayed films of 2H-MoS$_2$, graphene and In$_2$Se$_3$ (LPE) on PET. The films are ~3 cm × 3 cm. (b,c) SEM micrographs of the sprayed 2H-MoS$_2$ film. (d,f,g) Spatial absorbance at 550 nm of the sprayed films over a 3 cm × 3 cm region, step - 1 cm. (e) Optical absorbance at 550 nm of sprayed 2H-MoS$_2$ films as a function of the deposited ink volume (with absorbance from PET subtracted). Photo Credit: Guohua Hu, University of Cambridge and The Chinese University of Hong Kong.

Section S6. Optimization of printing parameters

As shown in Table S1, the formulated inks are characterized with a typical surface tension of ~28 mNm^{-1}, viscosity of ~2 mPas and density of ~0.8 gcm^{-3}, allowing the determination of a typical Z value of ~10, well within the optimal value range 1-14 for stable jetting. Indeed, during inkjet printing, we can observe stable jetting of single droplets from the printer stroboscopic camera (demonstrated with the 2H-MoS$_2$ ink); Fig. S8a. We control the dried droplet radius r' with varied substrate temperatures; Fig. S8b. As discussed, ideally the impingement of a droplet onto a pre-defined pattern should cause neither overspreading nor insufficient merging with neighboring droplets (*56*). Assuming a track of ink droplets (volume V') is printed in such an ideal case, the droplets then merge and form a line with uniform edges. Fig. S8c schematically shows a droplet impinging to this line with spacing of d'. Before solvent evaporation, the droplet has a spherical-cap geometry with radius of r', while the line has a cylindrical-cap geometry with radius of R'. The spherical-cap can be defined as:

$$V' = \frac{4}{3}\pi r'^3 \delta \tag{2}$$

where δ is the volume correction factor. Note that δ is expected to be very small when the droplet wets the substrate well, i.e. forms a small contact angle. On the other hand, δ approaches 1 for contact angles close to 180°. If d' is optimal, the impingement is then ideal such that the droplet extends the line by d' while the radius of the line remains R'. The cylindrical-cap is then defined as:

$$\frac{V'}{d'} = \pi R'^2 \delta' \tag{3}$$

where δ' is the volume correction factor for cylindrical-cap. Therefore, the relationship between R' and r' is:

$$\frac{R'}{r'} = \sqrt{\frac{4\delta}{3d'/r'\delta'}} \tag{4}$$

In addition, as shown in Fig. S8c, the impinging distance from the droplet to the end of the line (defined herein as the 'bead') is:

$$D' = d' - R' \tag{5}$$

Therefore, the relationship between D' and r' is:

$$\frac{D'}{r'} = \frac{d'}{r'} - \sqrt{\frac{4\delta}{3d'/r'\delta'}} \tag{6}$$

The morphologies of the printed patterns are governed by the droplet impinging behavior, which is essentially defined by the above parameters. As depicted in Fig. S8d, when d' is excessively small ($d' < R'$, i.e. $D' < 0$ from equation 5), the droplet lands on the bead of the line and expands around the bead rather than creating its own contact line, forming 'stacked coins' or 'bulged' line morphologies. However, when d' is large ($2R' < d' < 2r'$, i.e. $D' > R'$ from equation 5), the impinging of the droplet with the bead is restrained, forming 'scalloped' lines. For excessively large d' ($d' > 2r'$), the droplet does not impinge onto the line, forming 'isolated droplets'. For d' values between the bulged and scalloped scenarios (i.e. $0 < D' < R'$), the droplet impinges onto the bead and forms contact line with uniform edges.

Fig. S8f,g present respective printed lines of 2H-MoS$_2$ on Si/SiO$_2$ with single print repetition with variable d' and varied r'. Indeed, as shown, varying d' and r' for the 2H-MoS$_2$ ink produces vastly different morphologies, varying from stacked coins, bulged lines, uniform lines, scalloped lines and eventually to isolated droplets. For the r' ~34 µm case in Fig. S8f, the line with uniform edges begins to emerge when d' is 35 µm, and the line width is ~76 µm (i.e. R' is ~38 µm). Using the empirically obtained parameters above (r' ~34 µm, R' ~38 µm, d' = 35 µm) and V' of 10 pL (defined by the ink cartridge used in this work), the correction factors δ and δ' in equation 2 and equation 3 are determined, giving δ/δ' as 0.96. The normalized R' and D' values as a function of normalized d' (equation 4 and equation 6, respectively) are therefore plotted in Fig. S8e. Considering the above boundary condition for uniform line edges, $0 < D' < R'$, this suggests that the printed morphology with uniform line edges can be found when d'/r' is ~1.1-1.7. We note that similar studies of such droplet impingement behavior have been previously carried out with metal nanoparticle based inks (*56*).

The peak-to-peak edge roughness ($\Delta d'$) along the printed lines is a key consideration for the morphology of printed patterns. Here, we define the edge roughness as $(L_a - L_b)/2$, where L_a and L_b are the maximum and minimum width of a printed line, respectively. Fig. S8h replots the bulged line defined at 25 µm, where the maximal width L_1 is ~119 µm and the minimal width L_2 is ~108 µm. The roughness therefore is calculated as $(L_1 - L_2)/2 = (119 - 108)/2$ µm = 5.5 µm. For the scalloped line defined at 55 µm in Fig. S8i, L_3 and L_4 are ~78 µm and ~62 µm, respectively. The roughness is calculated as $(L_3 - L_4) 2 = (78 - 62)/2$ µm = 8 µm.

Having defined the edge roughness, we also confirm the above optimal printing parameters experimentally. Fig. S9a presents a contour plot of the edge roughness with respect to d' and r'. We consider $\Delta d'$ <2 µm as the criterion for uniform line edges. Fig. S9a shows that the 'uniform edges' region has distinct boundaries to the bulging and scalloping regimes, suggesting that the optimum d'/r' ratio obtained empirically is ~1.0-1.6, correlated with the above prediction and other ink systems such as polymer based and metal nanoparticle based inks (*56, 57*). This therefore suggests a general printing guidance for our formulated ink: the droplet spacing should be set as ~1.0-1.6 the deposited droplet radius for optimal printed morphologies. We note that the stacked coins region can also be exploited to print lines with uniform edges, but with larger width of the printed lines.
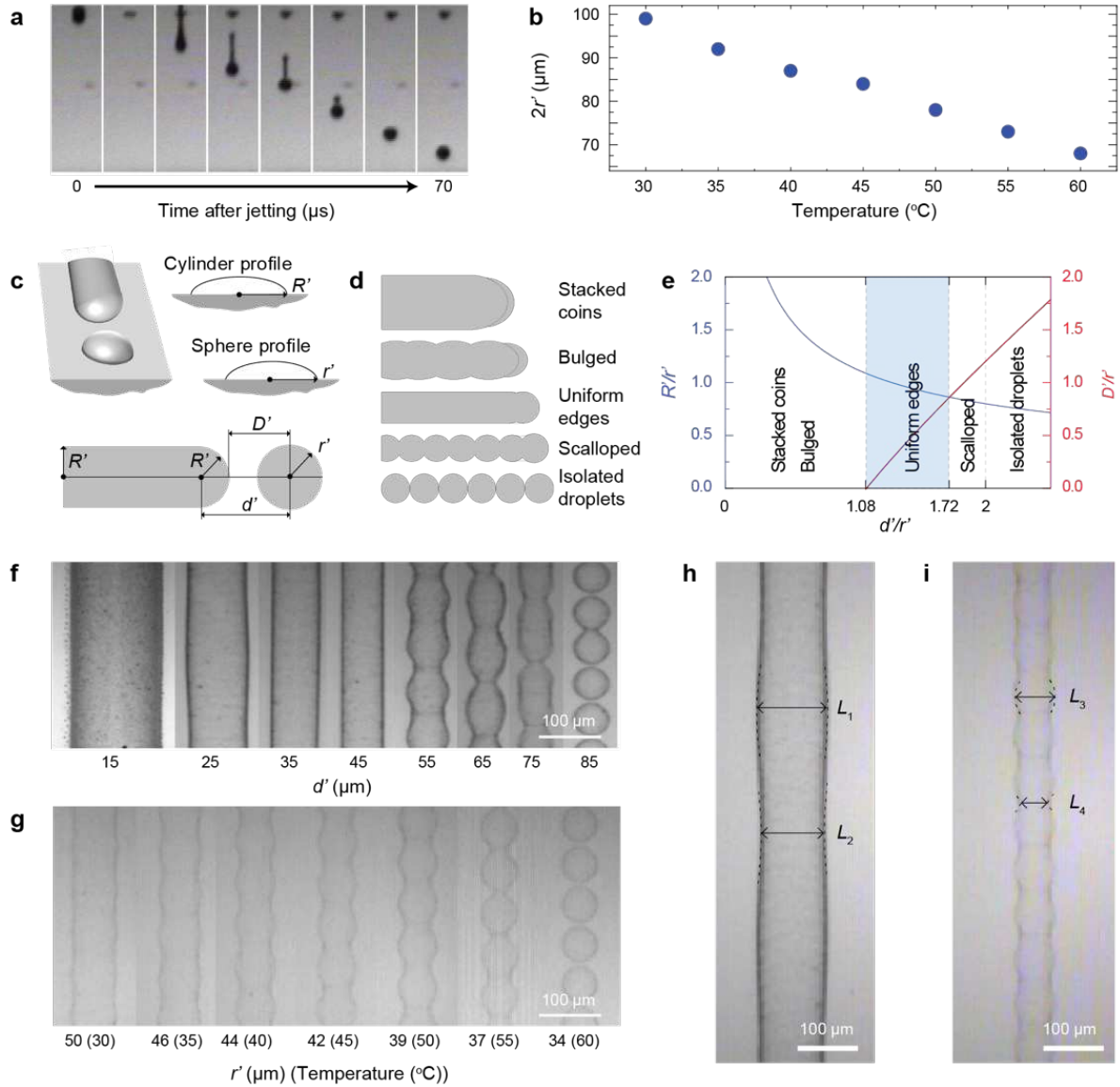
Fig. S8. Inkjet printing with the formulated inks in this work. (a) Ink droplet jetting sequence observed through the printer stroboscopic camera. (b) Radius (r') of dried 2H-MoS$_2$ ink droplets on Si/SiO$_2$ with respect to the substrate temperature. (c) Schematic figure with top view showing a droplet of a radius of r deposited to a defined cylindrical-cap line of a radius of R' with a droplet spacing of d'. (d) Schematic figures showing printed morphologies defined at varied droplet spacings. (e) Dimensionless R' versus d' plot predicting that printed morphology with uniform line edges is achieved when d' is 1.1-1.7 of r'. Photographs of typical printed lines with single print repetition under (f) varied d', r' is 34 µm, and (g) varied r', d' is 85 µm. Printed lines on Si/SiO$_2$ with d' of (h) 25 µm and (i) 55 µm, with 34 µm r'.
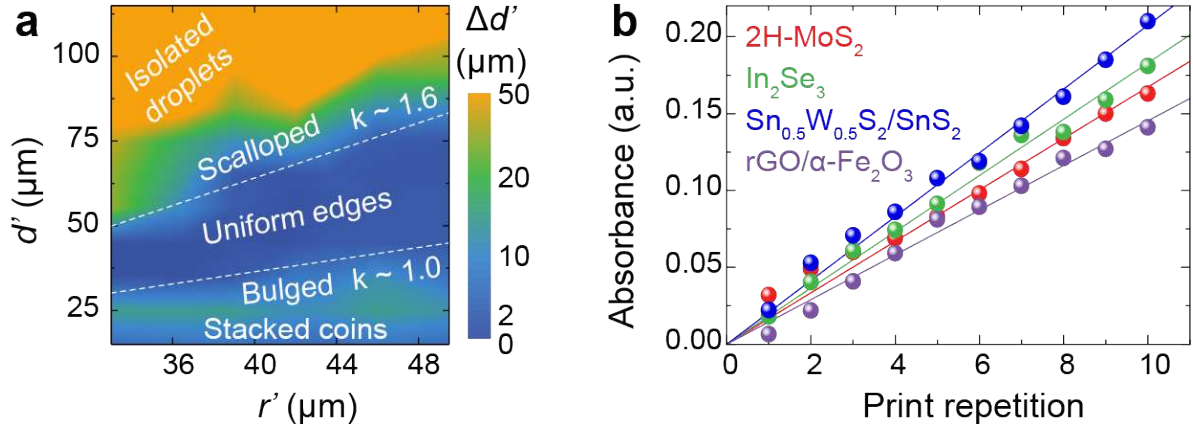
Fig. S9. Edge roughness of printed lines and optical absorbance of printed patterns. (a) Measured line edge peak-to-peak roughness $\Delta d'$ of the inkjet-printed $2H$-MoS_2 lines on Si/SiO_2 with respect to d' and r', showing uniform edges with $\Delta d' < 2$ μm are defined with $d'/r' \sim 1.0$-1.6. (b) Under the optimal printing parameters, the measured optical absorbance of some types of printed 2d crystals on glass with respect to print repetition at 550 nm, showing slope errors of 2.5%, 1.6%, 1.4% and 1.9%. Glass absorbance is subtracted.

Section S7. Inkjet-printed nonlinear optical devices

As presented in the manuscript, we first focus on small-scale fabrication of 2d crystal-based nonlinear optical devices, which are critical components for the development of ultrafast lasers. Such ultrafast laser technology continues to have a major impact in, for example, the observation of fast processes in nature as well as in industrial laser manufacturing and biomedical imaging (*58*). The high nonlinear susceptibilities and ultrafast carrier dynamics of a wide variety of 2d crystals, including those of 2H-MoS$_2$, are promising for the development of fast nonlinear optical switches known as saturable absorbers (SAs), which can be inserted into laser cavities to convert a low-power continuous-wave output into a train of high-peak-power ultrashort pulses (*22*). The properties of these ultrashort pulses are affected by the characteristics of the SA and hence it is of primary importance to have high device-to-device consistency. The demonstrated scalable patterning capability of our inks, in particular uniform flake distribution and precise control over the optical density, is ideal to deliver printed 2d crystal based SA fabrication.

Fig. S10a presents a photograph of an array of inkjet-printed 2H-MoS$_2$ SAs, highlighting high spatial consistency and uniformity. For printing of the SAs, the 1.5 μm thick PET is used directly as provided without any surface treatment. For ease of handing, this PET is laminated onto a 100 μm thick PET before printing; it can be easily peeled off for device integration after printing. Spatial color intensity (I_c) is then extracted for detailed investigation (Fig. S10b). To do this, we convert this photograph into a data worksheet of color intensity using OriginLab with the 'Matrix: Covert to Worksheet' function. The extracted data of the background is normalized to 0, whereas the maximum spike data-point across the SA region is normalized to 1. This spatial color intensity mapping shows that the normalized I_c is consistent within each individual SA and without discernible variations across the investigated SAs. The average I_c across the SA array is 0.811 ± 0.023, giving an area-to-area standard deviation of ~2.8%. We then characterize the nonlinear optical properties of the inkjet-printed 2H-MoS$_2$ SAs using an open-aperture Z-scan set-up (Fig. S10c). The acquired Z-scan datasets are well fitted with a two-level saturation model: $\alpha(I) = (\alpha_l - \alpha_{ns})/(1 + I/I_{sat}) + \alpha_{ns}$ (*59, 60*), where α_l is the linear absorption at low intensity and α_{ns} is the nonsaturable absorption at high intensity, I is the instantaneous incident intensity, and I_{sat} is the saturation intensity. The modulation depth (α_m) of a device is given by: $\alpha_m = \alpha_l - \alpha_{ns}$. Consequently, I_{sat} can be defined as the intensity required to reduce the absorption $\alpha(I)$ to $\alpha_l - (\alpha_m/2)$. The acquired spatial optical properties are highly consistent, with linear absorption (α_l) of 6.9 ± 0.13%, non-saturable absorption (α_{ns}) of 4.5 ± 0.22%, modulation depth (α_m) of 2.38 ± 0.11%, and saturation intensity (I_{sat}) of 3.37 ± 0.11 MWcm^{-2}. The properties of inkjet-printed SAs of WS$_2$ and MoSe$_2$ are shown in Fig. S11a,b. The spatial saturation intensities are 2.26 ± 0.14 MWcm^{-2} and 3.27 ± 0.13 MWcm^{-2} for WS$_2$ and MoSe$_2$, respectively. The spatial optical linear absorptions are 8.4 ± 0.10% and 8.2 ± 0.10%, respectively. The spatial optical non-saturable absorptions are 6.6 ± 0.22% and 5.3 ± 0.17%, respectively. The spatial optical modulation depths are 1.59 ± 0.20% and 2.9 ± 0.16%, respectively. This demonstrates that the inkjet-printed TMD SAs are highly uniform in the linear and nonlinear optical properties, with <5% standard deviation, suggesting that all the functional properties of the inkjet-printed SAs are spatially consistent.

The schematic erbium-doped (Er-doped) fiber laser set-up as in Fig. 4a is replotted with detail in Fig. S10d. The laser cavity consists of a single-clad Er-doped active fiber (YOFC EDF7/6/125-23, 4.8 m length, 17.8 ps^{2}km^{-1} group velocity dispersion (GVD)), co-pumped by a 980 nm laser diode through a 980/1550 wavelength division multiplexer (WDM), a polarization independent isolator (ISO) to ensure unidirectional propagation, a polarization controller (PC) to enable a continuous

adjustment of the net cavity birefringence and a 20:80 fused fiber output coupler (OC) for both spectral and temporal diagnostics. The ISO, PC and OC are fiber-pigtailed with single-mode fiber (SMF) with a GVD of -22 ps^2km^{-1}, while the WDM comprises single-mode HI1060 with a GVD of -7 ps^2km^{-1}. The entire cavity length is 10.18 m with a net cavity dispersion of 0.078 ps^2, which permits the laser to operate in the dispersion-managed soliton regime (*61, 62*).

When in operation, the SAs allow stable, self-starting mode-locked high-peak-power femtosecond pulses to be generated. Fig. S10e presents a typical autocorrelation trace of the generated pulses. We then measure the laser operation stability of the 16 randomly selected 2H-MoS$_2$ SAs from this array. The SA devices are integrated into the laser using a free-space configuration, such that we can change the sample without mechanically perturbing the cavity fiber which could induce change in the laser operation stability by varying the birefringence. This is achieved with an imaging system using a pair of 10 mm focal length lenses, where the SA devices are held at the focal point on a precision translation stage. Light transmitted through the device is collected by a second pair of 10 mm lenses and coupled back into fiber. Assessment of 16 individual SAs shows uniform pulse duration (τ) distribution, with 68.8% SAs within 1σ (3.3% spread from the μ value) and 100% finished device yield (Fig. 4c). We argue that the spread of τ is within acceptable statistical process variations for scalable manufacturing of ultrafast lasers, addressing a major limitation of solution-processed 2d crystal based nonlinear optical devices in the past decade (*22, 63*).

Besides the discussion in the manuscript, the measured generated ultrashort pulses from the 2H-MoS$_2$ SAs are presented in Fig. S10e,f. The corresponding spectral profiles also exhibit a high uniformity in laser operation: the position of the fundamental radio frequency spectra is 20.1755 ± 0.0016 MHz (0.0079% standard deviation) (Fig. S10g); the pulses are centered at 1558.46 ± 0.44 nm (0.03% standard deviation), with a full width at half maximum of 28.11 ± 0.39 nm (1.4% standard deviation) (Fig. S10h,i).

The inkjet-printed SA devices of WS$_2$ and MoSe$_2$ are also integrated into the Er-doped ultrafast fiber laser cavity for ultrashort laser pulse generation. Typical respective output pulse properties are shown in Fig. S11c,d. By incorporating WS$_2$ and MoSe$_2$ SAs into the laser cavity, the measured spectral FWHM is 27.59 nm and 27.85 nm, centered at 1558.66 nm and 1558.42 nm, respectively. The deconvolved pulse durations are 166.43 fs and 163.67 fs, respectively. The radio frequency spectra also show high signal-to-noise ratios, exceeding 60 dB.
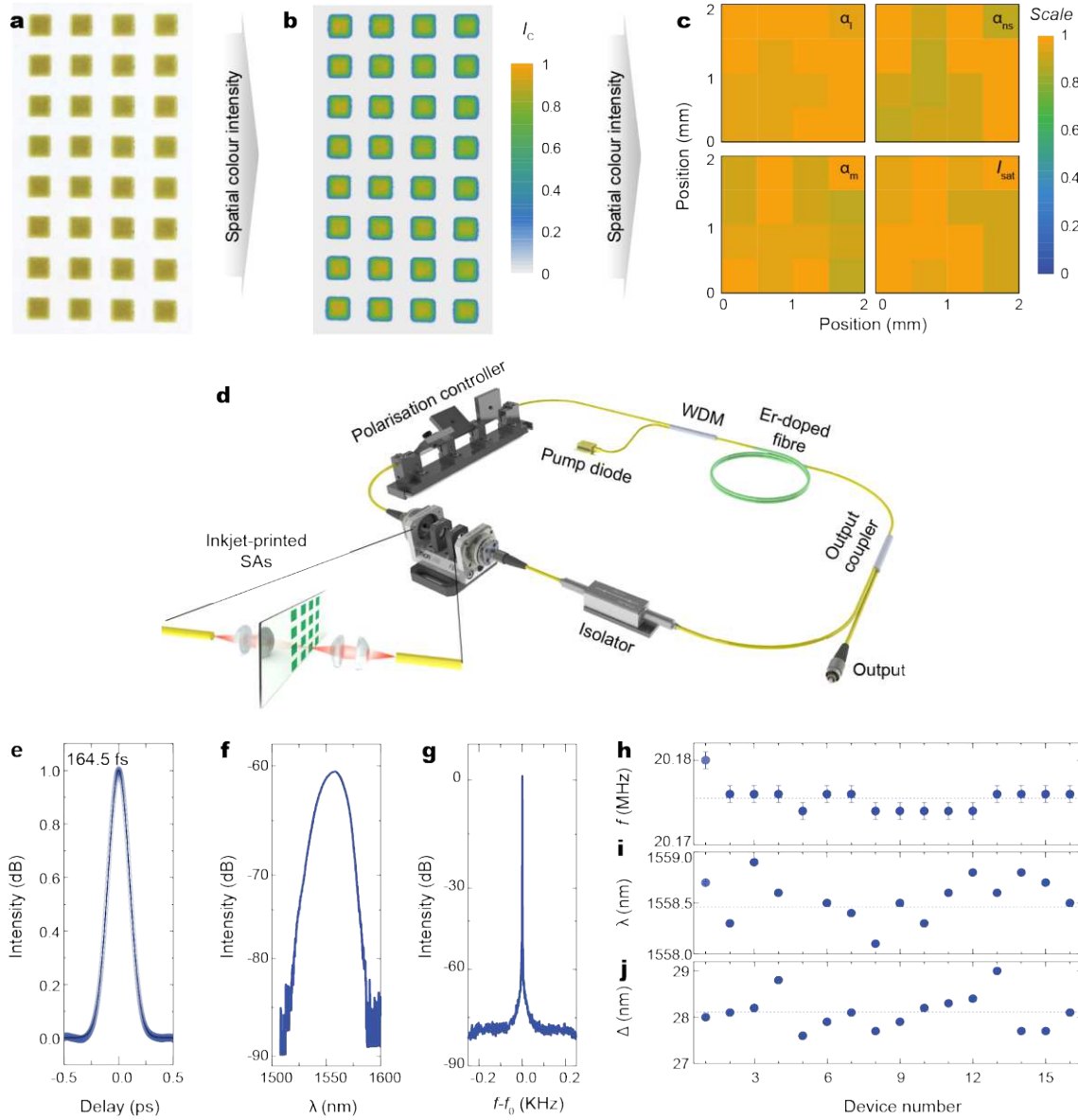
Fig. S10. Inkjet-printed MoS₂ nonlinear optical devices. (a) Photograph of inkjet-printed 4×8 2H-MoS₂ SA array on ultrathin PET (thickness 1.5 μm, laminated onto 100 μm thick PET), the background is paper, and (b) its spatial color intensity (I_C). The dimension of individual SAs is 2 mm × 2 mm, the color intensity of the background is normalized to 0 and the intensity of the maximum spike is normalized to 1; (c) Normalized spatial optical linear absorption (α_l, %), non-saturable absorption (α_{ns}, %), modulation depth (α_m, %) and saturation intensity (I_{sat}, MWcm^{-2}) of typical 2H-MoS₂ SAs, data acquired by Z-scan at 1560 nm, spatial step - 0.5 mm. (d) Schematic figure of the Er-doped ultrafast fiber laser cavity. (e) Autocorrelation trace of typical generated ultrashort pulses fitted with a Gaussian curve. (f) Typical output laser pulse spectra and (g) radio frequency spectra at the cavity fundamental repetition frequency (f_0; 20.176 MHz) of the 2H-MoS₂ SAs. (h) Measured position of the fundamental radio frequency spectra, (i) measured spectral central wavelength (λ), and (j) full width at half maximum (Δ) of the ultrashort pulses generated from 16 individual 2H-MoS₂ SA devices. The dashed lines indicate the average values, and the error bars indicate the errors from the measurement system.
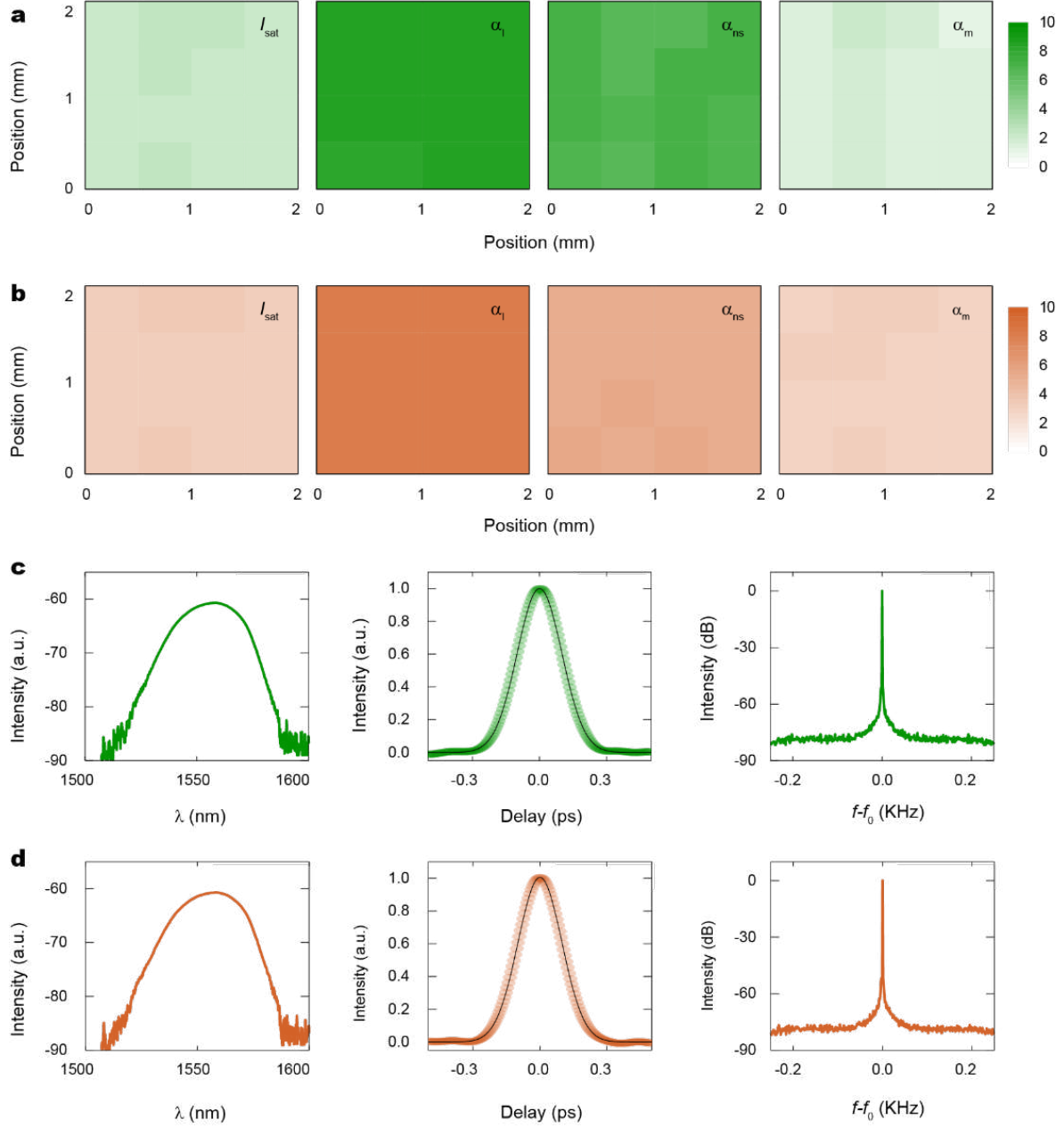
Fig. S11. Inkjet-printed WS₂ and MoSe₂ nonlinear optical devices. Spatial saturation intensity (I_{sat}, MWcm^{-2}), optical linear absorption (α_l, %), optical non-saturable absorption (α_{ns}, %), and optical modulation depth (α_m, %) at 1560 nm of typical inkjet-printed SAs of (a) WS₂ and (b) MoSe₂ over a 2 mm × 2 mm region, spatial step - 0.5 mm. Ultrafast laser operation of the inkjet-printed (c) WS₂ and (d) MoSe₂ SAs: output laser pulse spectra, autocorrelation trace of output pulses fitted with a Gaussian curve, and radio frequency spectra at 20.176 MHz.

Section S8. Inkjet-printed gas sensors

We also investigate large-scale manufacturing of gas sensors. Sensors find widespread uses in environmental monitoring, industrial processes, agriculture, smart buildings and increasingly, healthcare. As a material platform, rGO/α-Fe$_2$O$_3$ offers high sensitivity towards NO$_2$ at room-temperature and hence is promising for such sensor developments (*23*). More importantly, as demonstrated, rGO/α-Fe$_2$O$_3$ can be formulated into inkjet printable ink and deliver highly uniform and consistent deposition through our formulation. We believe this represents an important avenue towards high sensitivity, simple and cost-effective sensor fabrication of rGO/α-Fe$_2$O$_3$ and similar functional materials.

Fig. 4e in the manuscript shows an array of 50 fully-inkjet-printed rGO/α-Fe$_2$O$_3$ sensors. In these sensors, the inkjet-printed rGO/α-Fe$_2$O$_3$ onto interdigitated silver electrodes (Ag IDEs) acts as the active sensing layer. We use PET with a porous coating that is specifically designed for silver printing, to avoid short-circuits of the Ag IDEs that are otherwise seen with PET substrates (Fig. S12a,b). Optical microscopy shows highly uniform deposit of rGO/α-Fe$_2$O$_3$ over the Ag IDEs; Fig. 4e. When exposed to NO$_2$, the printed sensors show a strong response, even at concentrations down to 200 ppb. The average (maximum) responsivity (R_{gas} - the change in the device resistance) is ~24% (~37%) over the investigated concentration range (200-1,000 ppb, in steps of 200 ppb); Fig. S12c. We then assess the device-to-device consistency in R_{gas}. For this, we measure the maximum R_{gas} at 1 ppm NO$_2$ of this sensor array (3 out of the 50 devices are short-circuited during electrode fabrication using inkjet printing of silver inks), and find that 78.7% sensors are within $\pm$ 1σ (2.5% spread from their μ value); Fig. S12c, Fig. 4g. Note that the baseline drift, common for chemiresistive sensors, can be addressed by saturating the sensors in NO$_2$; Fig. S12d. This demonstration reinforces the fact that our formulation enables scalable device manufacturing through inkjet printing with high device-to-device consistency.
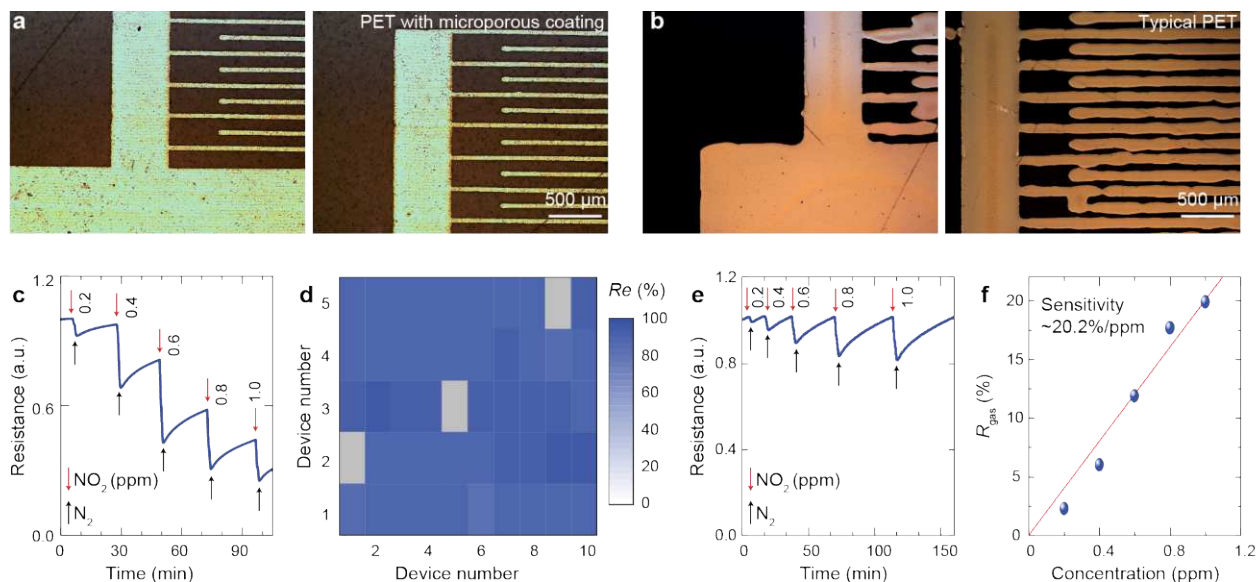
Fig. S12. Inkjet-printed rGO/α-Fe₂O₃ gas sensors. Optical micrographs of inkjet-printed commercial silver (Sigma) interdigitated electrodes at different regions on (a) the Mitsubishi silver printing PET substrate with porous coating, and (b) regular PET substrate. (c) Typical measured response under exposure to NO_2 in the initial measurement cycles. (d) Mapping of the measured responsivities (R_{gas} – the change in the device resistance) to 1 ppm NO_2 of the all-inkjet-printed rGO/α-Fe₂O₃ sensor array shown in Fig. 4d in the manuscript. The 'null' grey spots represent short-circuited devices. (e) Typical measured stabilized response under exposure to 1 ppm NO_2 for 30 min. (f) The measured stabilized R_{gas} as a function of NO_2 concentration, giving a stabilized sensitivity of 20.2% per ppm to NO_2.

Section S9. Inkjet-printed photodetectors

Semiconducting TMDs are an interesting material platform for the photodetector development due to their transition bandgap spanning the visible to near-infrared (NIR) wavelength region (*1*). Towards cost-effective real-world device manufacturing, inkjet printing of TMDs has been successfully exploited in laboratorial photodetector demonstrations (*6, 64, 65*). However, challenges exist. The scalability is significantly hindered (≤20 devices) due to the limitations in the solution-processed 2d crystal dispersions, and as such a rigorous characterization of device-to-device variations was not been performed. The devices, based on solution-processed TMDs, also show pretty poor performances compared to the ones based on micro-mechanically cleaved and chemical vapor deposition-grown materials. Practical applications therefore require further substantially improved ink formulation and materials functionality. Nevertheless, with a highly controlled and uniform deposition capability, our ink formulation solves the challenge of scalable device fabrication, meeting the needs for wafer-scale manufacturing.

Towards this goal, we demonstrate 4,500 (100 × 45) 2H-MoS$_2$ photodetectors by inkjet printing 2H-MoS$_2$ onto interdigitated gold electrodes on a single silicon wafer; Fig. 4h. As shown, the printed 2H-MoS$_2$ array is visually highly identical and consistent; Fig. 4i. Fig. 4j,k are zoomed-in optical and false-colored SEM images of a single device and the printed 2H-MoS$_2$, respectively, showing an even flake distribution over the electrodes. To assess the device-to-device consistency of the wafer-scale photodetectors shown in Fig. 4h in the manuscript, we stochastically measure the electrical conductance (*G*) of 165 individual devices across the entire array (Fig. S13a). Our measurements confirm that 61.2% (101 out of 165) of the devices have *G* values within ± 1σ (11.3% spread from the μ value), with 161 out of 165 (97.6%) within the 2σ range (Fig. S13b), again highlighting high device-to-device consistency and manufacturability using our ink formulation. As opposed to this, an array of 5 × 10 2H-MoS$_2$ photoreactors fabricated using the solution-processed NMP based dispersion (discussed in Fig. 1a) shows uncontrollable, varied print patterns of MoS$_2$ with uneven flake distribution over the electrodes; Fig. S14a,b. This leads to a significantly wider spread in the *G* values across the device array; Fig. S14c. Gaussian fitting gives a 29.1% spread for 1σ from the μ value; Fig. S14d.

We then characterize the photoresponse of the printed photodetectors. As shown in Fig. S13c, compared to the dark current, the current under excitation is typically over one order of magnitude larger, with responsivity (R_{photo}) of up to 150 μAW^{-1}. Fig. S13c presents the typical photoresponse with respect to time, showing that the current under excitation remains stable, with <5% error. After confirming the stable device operation, as discussed, we then investigate the device-to-device consistency in terms of R_{photo}. As presented in Fig. S13d and Fig. 4i, R_{photo} from a randomly-selected 5 × 10 device array is highly consistent (6 out of the 50 devices are short-circuited during electrode fabrication using lithography), with 68.2% of the devices within ± 1σ (9.1% spread from the μ value) range, and 97.7% within ± 2σ which we believe is sufficient for industrial-scale manufacturing. The above demonstrations envisage the prospect of our ink formulation of 2d crystals, their heterostructures and hybrids in real-world wafer-scale manufacturing with highly consistent device-to-device performance.

Fig. S15a,c present the mapping of measured R_{photo} values under 40 μW excitation at 5 V for WS$_2$ and MoSe$_2$ photodetector arrays (50 devices), respectively. As shown, the measured R_{photo} values for the WS$_2$ photodetectors are highly consistent. Their measured R_{photo} values can also be well-fitted with Gaussian distribution, with fitted μ and σ of 2.6 μAW^{-1} and 0.3 μAW^{-1}, respectively; Fig. S15b. Therefore, 100% of the measured R_{photo} values are distributed within ± 3σ. The

measured R_{photo} values for the MoSe$_2$ photodetectors, however, show large variations. Fig. S15d presents typical time response of MoSe$_2$ photodetector, showing that the current decreases upon light excitation. We propose that the large R_{photo} variations of the MoSe$_2$ photodetector array are due to the instability of MoSe$_2$ but not the device fabrication strategy. Nevertheless, the R_{photo} of both the 2H-MoS$_2$ and WS$_2$ photodetector arrays exhibit high device-to-device uniformities.
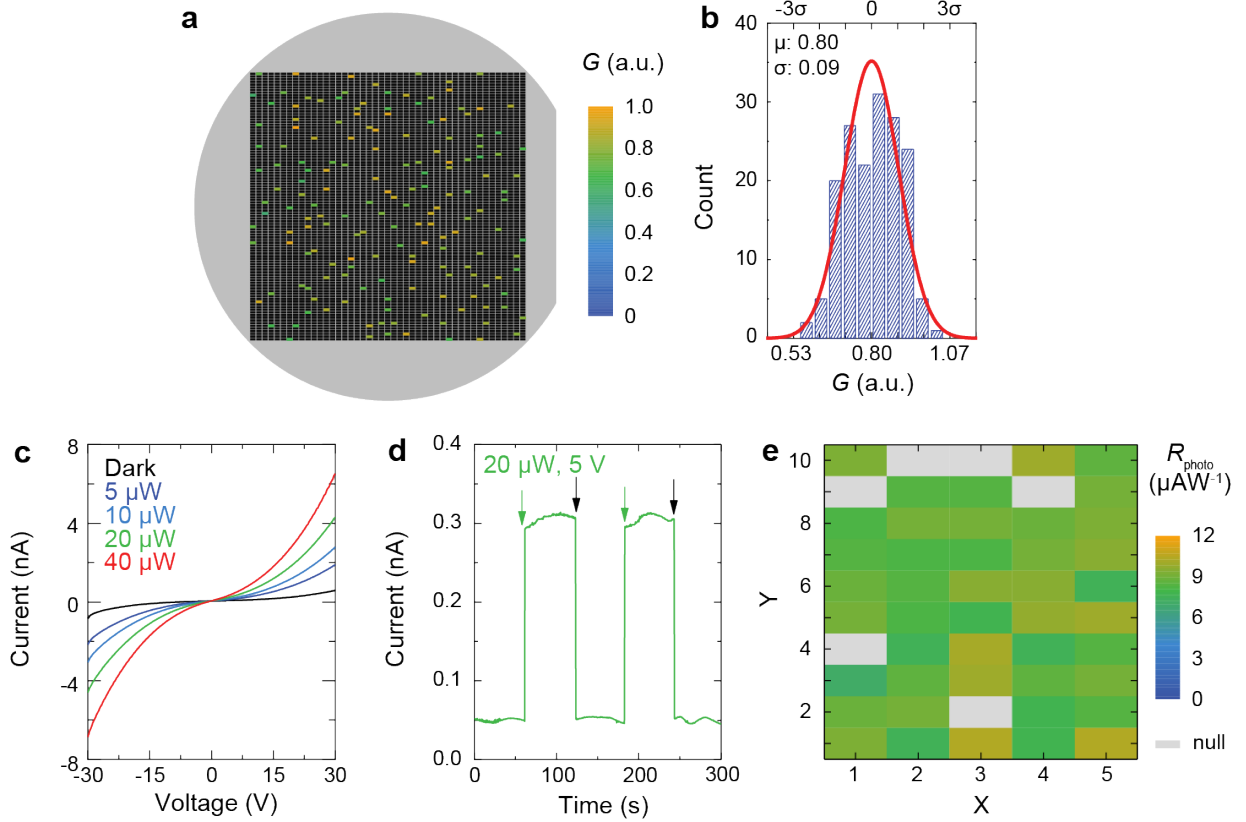

Fig. S13. Inkjet-printed wafer-scale MoS$_2$ photodetectors. (a) Normalized electrical conductance (G) map of the wafer-scale photodetectors shown in Fig. 4h in the manuscript, the spots indicate the measured devices. (b) Gaussian fitting of the measured G, with 101 out of 165 (61.2%) within $\pm 1\sigma$, 161 out of 165 (97.6%) within $\pm 2\sigma$, and 165 out of 165 (100%) within $\pm 3\sigma$. (c) Typical device current response to varied excitation powers. (d) Typical time response, bias 5 V, the green and black arrows indicate excitation on and off. (e) Responsivity (R_{photo}) map of a 50 device array under 40 μW, bias 5 V, the 'null' grey spots represent short-circuited devices. A 635 nm excitation laser is used.
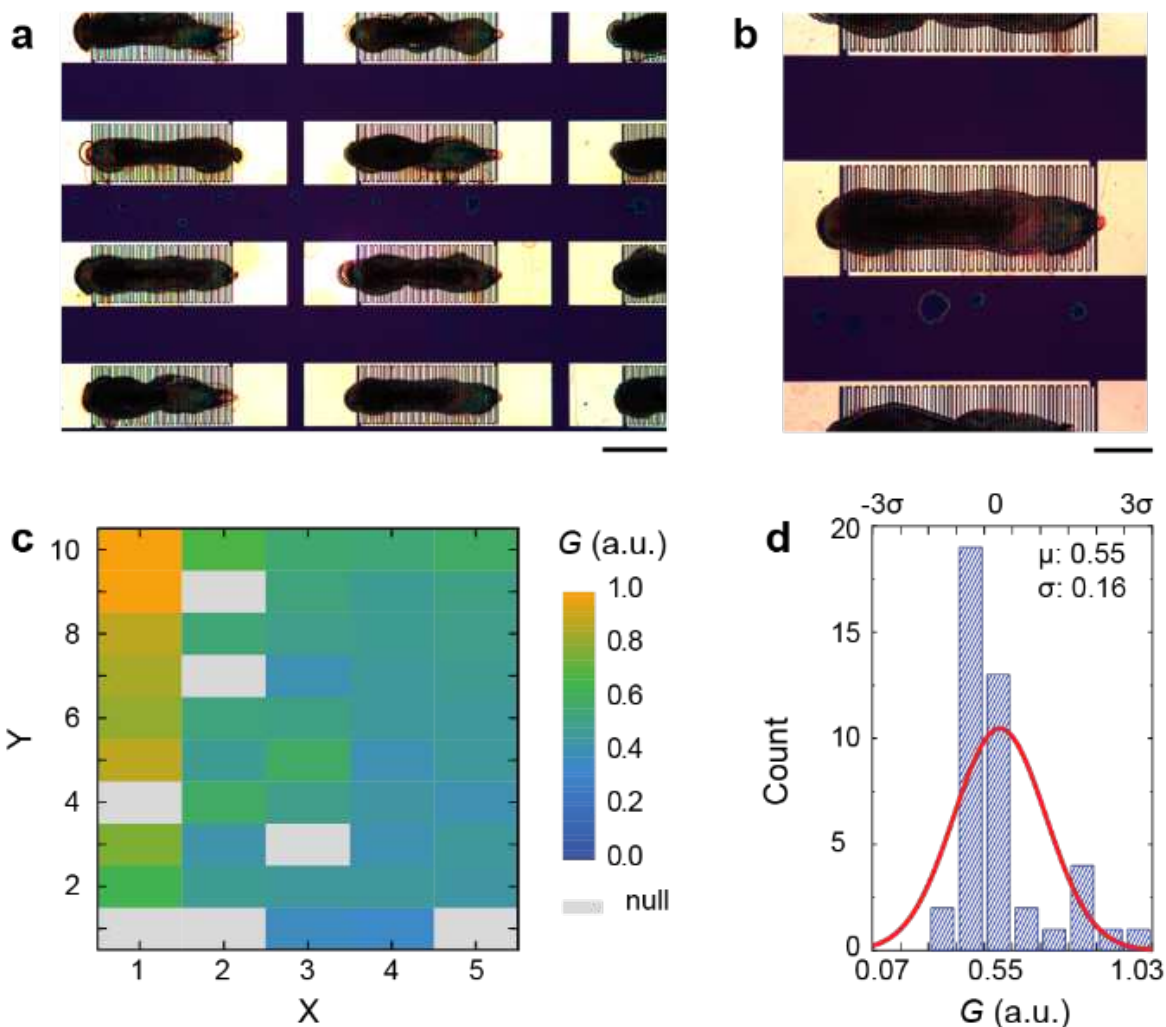
Fig. S14. Inkjet-printed MoS₂ photodetectors with the solution-processed NMP based dispersion. (a, b) Optical micrographs of 2H-MoS₂ photodetector devices fabricated using the as-produced NMP based dispersion discussed in Fig. 1a, showing uncontrollable, varied printed MoS₂ patterns with uneven flake distribution over the electrodes, respective scale bar 200 μm and 100 μm. (c) Normalized electrical conductance (G) map of the photodetector array printed with the NMP based dispersion, the 'null' grey spots represent short-circuited devices. (d) Gaussian fitting of the measured G values, showing a 29.1% spread from the μ value.
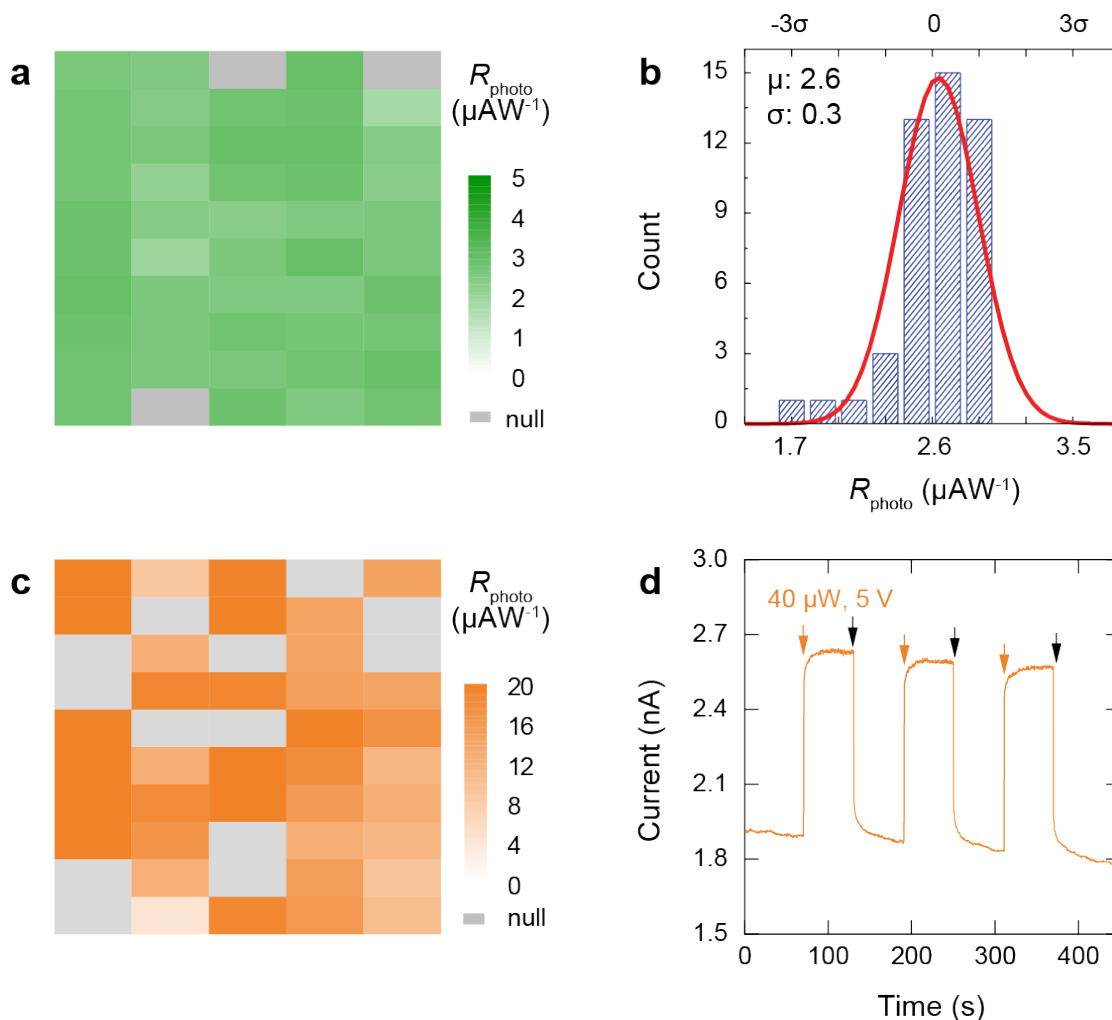
Fig. S15. Inkjet-printed WS$_2$ and MoSe$_2$ photodetectors. (a) Mapping of R_{photo} under 40 μW at 5 V for 50 WS$_2$ photodetector devices, and (b) the corresponding Gaussian fitting, with 37 out of 47 (78.7%) within ± 1σ, 45 out of 47 (95.7%) within ± 2σ, and 47 out of 47 (100%) within ± 3σ. 3 devices are short-circuited, represented by the 'null' grey spots. (c) Mapping of R_{photo} under 40 μW at 5 V for MoSe$_2$ photodetectors, and (d) the corresponding typical time response. The orange and black arrows indicate excitation on and off. The 'null' grey spots represent short-circuited devices. A 635 nm excitation laser is used.